Joule

Article

Flexible freestanding Ag_2Se thermoelectric films with high performance for sap flow monitoring

Graphical abstract

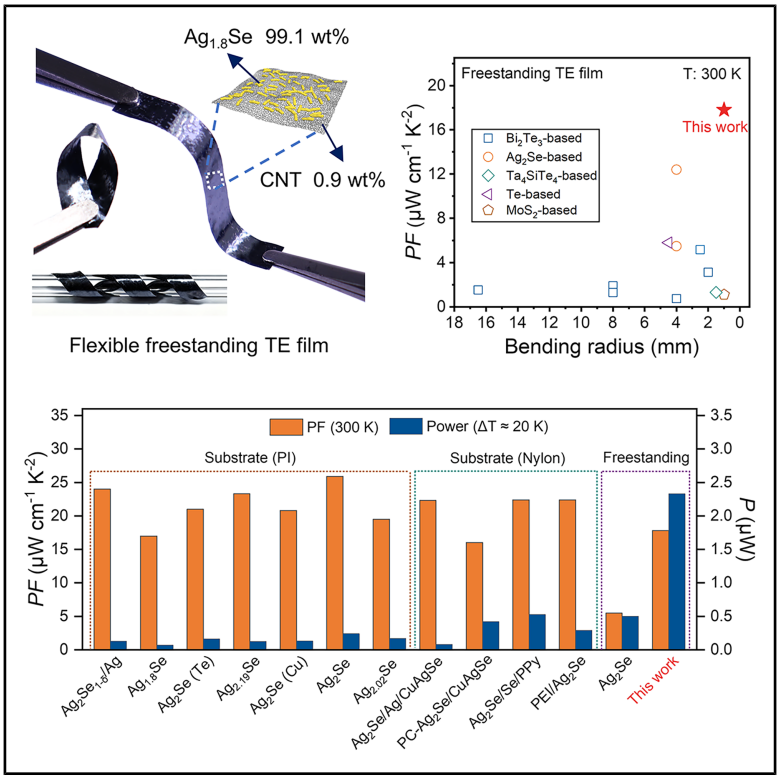

Highlights

- Freestanding $Ag_{1.8}Se$/CNT films endure 20,000 bending cycles at a 2-mm radius
- A power factor of 20.9 μW cm^{-1} K^{-2} at 380 K is achieved with ultralow CNT content
- A flexible TE generator delivers 4.6 μW cm^{-1} K^{-2} normalized power density
- A highly sensitive, self-powered TE sensor enables reliable plant sap flow monitoring

Authors

Gang Li (李钢), Xiang-Rui Guo (郭祥瑞), Tao Wang (汪涛), Jing Wang (王晶), Yu Wang (王瑜), Guangming Chen (陈光明), Yan-Qing Lu (陆延青)

Correspondence

yuwang87@nju.edu.cn (Y.W.), chengm@szu.edu.cn (G.C.), yqlu@nju.edu.cn (Y.-Q.L.)

In brief

Ultralow-content CNT (0.9 wt %) enables freestanding flexibility in $Ag_{1.8}Se$ while enhancing thermoelectric performance via energy filtering. The $Ag_{1.8}Se$/CNT films exhibit a high room-temperature power factor and small bending radius. The ~10-μm-thick freestanding films enable flexible devices with substantial power output. This strategy provides a sustainable route to high-performance inorganic thermoelectrics.

Li et al., 2026, Joule *10*, 102487
October 21, 2026
https://doi.org/10.1016/j.joule.2026.102487

CellPress

Please cite this article in press as: Li et al., Flexible freestanding Ag_2Se thermoelectric films with high performance for sap flow monitoring, Joule (2026), https://doi.org/10.1016/j.joule.2026.102487

Joule

CellPress

Article

Flexible freestanding Ag_2Se thermoelectric films with high performance for sap flow monitoring

Gang Li (李钢),[1] Xiang-Rui Guo (郭祥瑞),[1] Tao Wang (汪涛),[1] Jing Wang (王晶),[1] Yu Wang (王瑜),[1,3,*] Guangming Chen (陈光明),[2,*] and Yan-Qing Lu (陆延青)[1,*]

[1]National Laboratory of Solid State Microstructures, Key Laboratory of Intelligent Optical Sensing and Manipulation, College of Engineering and Applied Sciences, and Collaborative Innovation Center of Advanced Microstructures, Nanjing University, Nanjing 210023, China

[2]College of Materials Science and Engineering, Shenzhen University, Shenzhen 518055, China

[3]Lead contact

*Correspondence: yuwang87@nju.edu.cn (Y.W.), chengm@szu.edu.cn (G.C.), yqlu@nju.edu.cn (Y.-Q.L.)

https://doi.org/10.1016/j.joule.2026.102487

CONTEXT & SCALE Thermoelectric materials that can directly convert small amounts of heat into electricity are attracting growing interest for powering the Internet of Things and wearable electronics. The development of flexible thermoelectrics is particularly appealing because of their ability to conform to diverse heat sources, enable stable energy harvesting, and integrate seamlessly with soft electronic systems. However, most flexible thermoelectric materials today struggle to reconcile mechanical flexibility with high thermoelectric performance and substantial power output. In particular, flexible inorganic thermoelectric composites face a long-standing trade-off: high filler content enhances flexibility but sacrifices performance, whereas low filler content preserves performance at the expense of flexibility. Overcoming this inherent contradiction remains a central bottleneck in the field.

In this study, we overcome this limitation by engineering the microstructure of a new type of freestanding composite film composed of $Ag_{1.8}Se$ with a minimal amount of CNTs. Although the CNT content is very low, it forms an interconnected network that provides mechanical support and enhances electrical transport. This design enables the film to combine strong flexibility with high room-temperature thermoelectric performance. Surprisingly, the material retains nearly all of its performance after 20,000 bending cycles at a small radius of 2 mm, demonstrating its suitability for long-term use in wearable or deformable systems. When assembled into simple devices, these films can generate meaningful power from modest temperature differences and can be integrated onto biodegradable supports. This unlocks opportunities for sustainable and bio-interfaced electronics. We further show that the devices can attach directly to plant surfaces, enabling both high-sensitivity sap flow monitoring and self-sufficient energy supply. This design principle can be applied to other thermoelectric materials, offering a scalable and sustainable route toward high-performance flexible thermoelectrics.

SUMMARY

Flexible inorganic thermoelectrics are promising for the Internet of Things and wearable electronics. While solution processing offers a facile route to such materials, simultaneously achieving mechanical flexibility and substantial power output remains challenging. Here, we report a microstructure-engineering strategy to fabricate freestanding $Ag_{1.8}Se$/carbon nanotube (CNT) composite films with ultralow CNT content (0.9 wt %). An interwoven CNT network establishes dense, conductive interfaces with $Ag_{1.8}Se$ nanowires, enabling efficient carrier transport and exceptional flexibility. The ~10-μm films achieve a power factor of 20.9 $\mu W\ cm^{-1}\ K^{-2}$ at 380 K and retain >95% of their performance after 20,000 bending cycles at a 2-mm radius. An assembled flexible device delivers an output power of 15.4 μW and a normalized power density of 4.63 $\mu W\ cm^{-1}\ K^{-2}$ under a 50 K temperature gradient. Integrated with biodegradable supports, the devices demonstrate recyclability and enable sap flow monitoring. This facile and sustainable approach is generalizable to other systems such as Bi_2Te_3 and Cu_2Se.

Please cite this article in press as: Li et al., Flexible freestanding Ag_2Se thermoelectric films with high performance for sap flow monitoring, Joule (2026), https://doi.org/10.1016/j.joule.2026.102487

INTRODUCTION

In recent years, the rapid advancement of self-powered Internet of Things (IoT) and wearable electronics has driven growing interest in sustainable energy-harvesting technologies.[1,2] Flexible inorganic thermoelectric materials, which can directly convert low-grade body heat into usable electricity, represent a promising power solution for such applications because of their capacity for lightweight, sustainable power generation; close adherence to arbitrary heat sources; and silent operation.[3–5] Ideally, these materials should combine high thermoelectric performance, substantial power output, robust mechanical flexibility, low processing temperatures, low toxicity, and long-term stability.[1] Nevertheless, simultaneously fulfilling these criteria remains a significant challenge with current material systems. To improve output performance, it is crucial to optimize the figure of merit ($zT = S^2\sigma T/\kappa$) and the power factor ($PF = S^2\sigma$), where S, σ, T, and κ represent the Seebeck coefficient, electrical conductivity, absolute temperature, and thermal conductivity, respectively.[6,7] Beyond intrinsic thermoelectric properties, the effective power generation of thermoelectric devices is strongly determined by the material's thickness,[8,9] which governs internal resistance across the device. This interdependence underscores that the design of flexible thermoelectric materials requires optimizing their thermoelectric properties and thickness in a coordinated manner while ensuring sufficient mechanical flexibility to maximize power output.

The general method for creating flexible inorganic thermoelectric materials involves depositing inorganic layers (typically less than 1 μm thick) onto flexible polymer substrates through techniques such as magnetron sputtering, pulsed laser deposition, and screen printing.[5,8,10] However, these methods have inherent drawbacks; the submicron-thick films show high internal resistance and low power output (Figure 1A, left; Note S1), while the polymer substrates contribute to heat loss, ultimately reducing power density.[7,11,12] To address these issues, freestanding inorganic thermoelectric films have gained considerable interest as an alternative platform.[13] Recently, silver chalcogenides Ag_2X (X = S, Se, Te) have been demonstrated to be processable into ductile, freestanding thermoelectric films.[4,14,15] Still, their fabrication often depends on energy-intensive procedures. Despite progress in reducing metalworking temperatures, these methods are still limited by the essential step of high-temperature melting (Figure 1A, right).[16–18] An effective approach to bypass this problem is to create inorganic-carbon composite thermoelectric materials via solution-processing techniques such as vacuum filtration, drop-casting, and layer-by-layer assembly.[19–21] While adding conductive carbon frameworks can improve both mechanical flexibility and thermoelectric performance to some degree, current strategies still struggle to optimize both simultaneously.[22,23] Generally, a higher carbon filler content helps build a strong mechanical network but significantly hampers thermoelectric performance because of increased interfacial scattering and reduced carrier mobility.[24] On the other hand, low filler amounts can enhance the S and PF through interfacial energy filtering, but insufficient filler connectivity results in weak mechanical support and brittleness. Therefore, achieving a balance of excellent flexibility and high thermoelectric performance at ultralow carbon loadings remains a key challenge.

In this work, we report the facile fabrication of freestanding $Ag_{1.8}Se$/carbon nanotube (CNT) composite films, through vacuum filtration followed by hot pressing, which exhibit excellent flexibility, high PF, enhanced power output, and reduced processing temperatures (Figure 1B). We propose that synergistic enhancement of flexibility and thermoelectric performance at an ultralow CNT content (0.9 wt %) is achieved by precisely controlling the Ag/Se molar ratio and facilitating the stable, uniform dispersion of $Ag_{1.8}Se$ with CNT, using N, N-dimethylformamide (DMF) as a solvent. We show that the resulting film with a thickness of ~10 μm achieves a high PF of 20.9 μW cm^{-1} K^{-2} at 380 K, while it exhibits remarkable durability—maintaining over 95% of its performance after 20,000 cycles at a 2-mm bending radius. We fabricated an in-plane flexible thermoelectric generator (F-TEG) comprising five $Ag_{1.8}Se$/CNT legs connected in series, which delivers an outstanding output power (P) of 15.4 μW under a temperature difference (ΔT) of 50 K. With biodegradable poly(α-lipoic acid) (PLA) films as encapsulation layers, the developed flexible device showcases excellent recyclability, while the recovered materials retain outstanding performance stability. Finally, we successfully demonstrated that this device functions as a dual-purpose unit for both sensing and power generation in sap flow monitoring, establishing a versatile, efficient, and cost-effective solution for bio-interfaced applications.

RESULTS

$Ag_{1.8}Se$/ultralow-CNT-content composites

To achieve synergistic enhancement of thermoelectric performance and mechanical flexibility at low CNT filler contents, it is essential to precisely control the Ag_xSe-to-CNT ratio while ensuring uniform distribution of both components within the composite system. To accomplish these goals, we propose a strategy that combines optimization of the Ag/Se molar ratio with selection of an appropriate solvent to promote homogeneous dispersion of the nanocomponents. Following this strategy, we synthesized $Ag_{1.8}Se$ nanowires and prepared a composite solution in which $Ag_{1.8}Se$ and CNTs were uniformly dispersed using DMF as the solvent. We then successfully fabricated freestanding $Ag_{1.8}Se$/CNT composite films via a facile vacuum filtration approach followed by mild-temperature hot pressing (Figure S1).

By incorporating an ultralow-content CNT network (0.9 wt %) as a flexible conductive scaffold within an $Ag_{1.8}Se$ (99.1 wt %) matrix, the resulting composites exhibit high thermoelectric performance and excellent flexibility simultaneously (Figures 1C and S2). The uniform distribution of $Ag_{1.8}Se$ and CNT facilitates the formation of abundant, well-established $Ag_{1.8}Se$-CNT interfaces, leading to a pronounced interfacial energy-filtering effect that effectively decouples σ and S (Figures 1C, S3, and S4; Note S2),[22] yielding a remarkable PF at room temperature. Meanwhile, the percolating CNT network enhances charge transport and mechanical compliance, enabling the film to maintain stable thermoelectric performance even after repeated bending to a radius as small as 1 mm.

Please cite this article in press as: Li et al., Flexible freestanding Ag_2Se thermoelectric films with high performance for sap flow monitoring, Joule (2026), https://doi.org/10.1016/j.joule.2026.102487

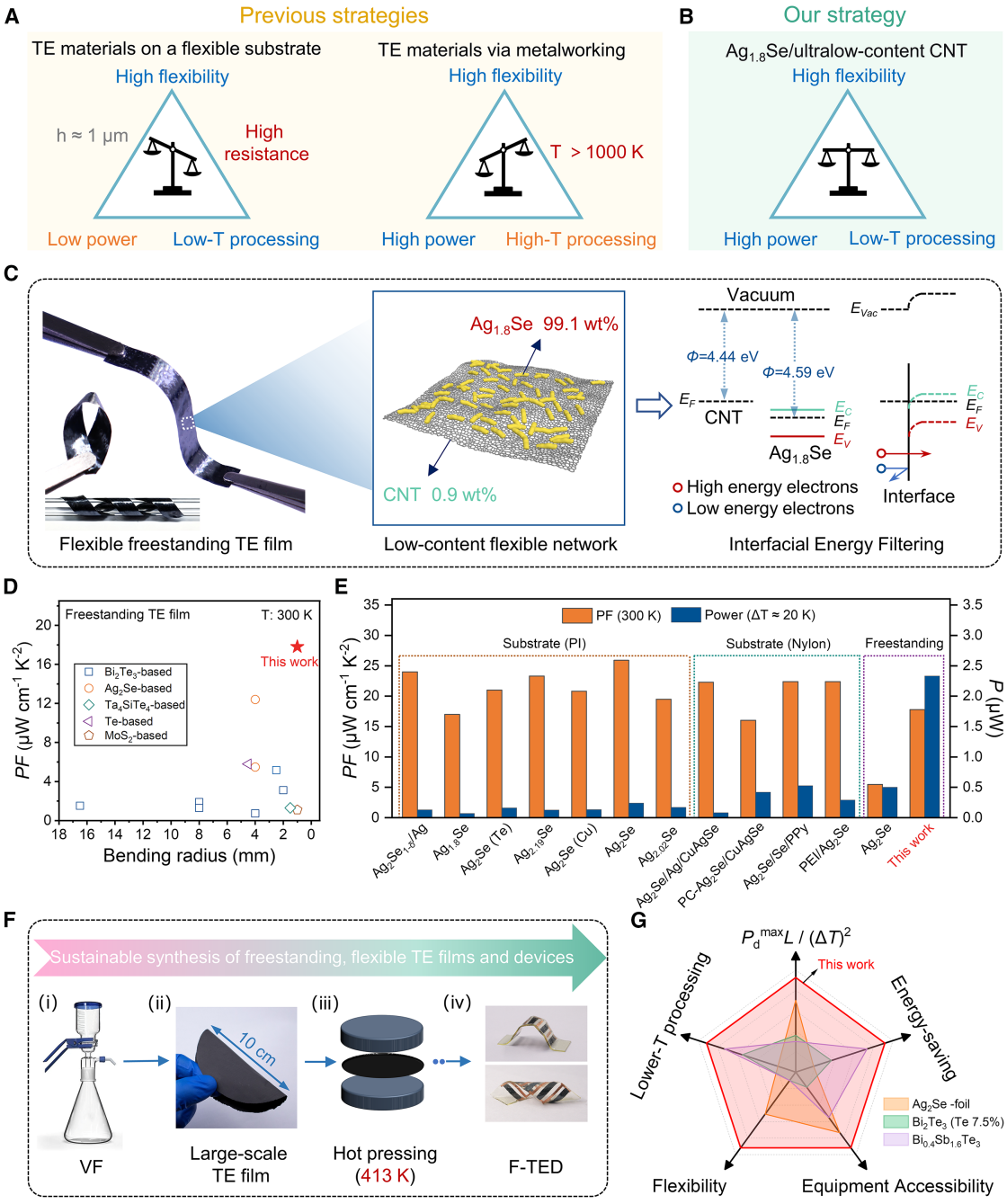

Figure 1. $Ag_{1.8}Se$/ultralow-CNT-content composite films and devices

(A and B) Schematic illustration comparing limited-power or high-temperature (high-T) processing via conventional approaches (A) with high-power and low-T processing via our proposed strategy (B) for preparing flexible inorganic thermoelectric (TE) films.

(C) Schematic illustration showing the structure and electron transport mechanism of $Ag_{1.8}Se$/CNT films. The inset shows a bent $Ag_{1.8}Se$/CNT film.

(D) Comparison of the *PF* and bending radius of freestanding TE films via solution processing, as reported in previous studies and this work.

(E) Comparison of *PF* of Ag_2Se-based TE materials and power of five devices (uniform length and width for each leg), as reported in previous studies and this work.

(F) The fabrication steps of the freestanding $Ag_{1.8}Se$/CNT film and the flexible TE device (F-TED): (i) vacuum filtration of the mixture of $Ag_{1.8}Se$ and CNT, (ii) the formation of a freestanding and flexible $Ag_{1.8}Se$/CNT film, (iii) hot-pressing processing at 413 K for 30 min to improve its density, and (iv) the assembling of the F-TED on a flexible and recyclable PLA film.

(G) Comparison of the multidimensional performance of this work with representative TE materials and devices. The plot's source data are provided in Table S4.

Please cite this article in press as: Li et al., Flexible freestanding Ag_2Se thermoelectric films with high performance for sap flow monitoring, Joule (2026), https://doi.org/10.1016/j.joule.2026.102487

Owing to this compelling combination of high *PF* and mechanical flexibility, the $Ag_{1.8}Se$/CNT freestanding film surpasses all flexible freestanding thermoelectric materials via solution processing (Figures 1D and S5; Tables S1 and S2).[19,25–33] A F-TEG constructed with five series-connected $Ag_{1.8}Se$/CNT legs delivers a *P* substantially exceeding that of its counterparts fabricated from thermoelectric materials deposited on flexible substrates. Despite the excellent *PF* of the materials used in these devices, their submicron-thickness structural design—necessary to maintain flexibility—limits the conversion of high material *PF* into effective device output, resulting in extremely low power levels (Figure 1E; Table S3).[30,34–44] Moreover, the fabrication of freestanding $Ag_{1.8}Se$/CNT composite films employs a mild hot-pressing annealing temperature (413 K) and requires neither complex nor costly equipment, thereby reducing energy consumption and enabling the fabrication of large-area films (Figures 1F and S6). The assembled devices can be readily transferred onto diverse substrates, providing enhanced design flexibility and facilitating integration with additional functionalities. A comparative analysis of state-of-the-art flexible thermoelectric materials, assessed based on power density, energy savings, equipment accessibility, flexibility, and processing temperature, underscores the advantages of our $Ag_{1.8}Se$/CNT composite platform (Figure 1G; Table S4).[5,16,45] This approach effectively balances flexibility, power generation, and mild-temperature processability (Figure 1B), providing a strong foundation for future use in self-powered wearable sensors and IoT devices.

Characterization of the composite films

To determine the optimal Ag/Se ratio for maximizing thermoelectric performance, we prepared a series of films with nominal compositions Ag_xSe/CNT (x = 1.0, 1.2, 1.4, 1.6, 1.8). We focused on $x < 2$, as freestanding films are difficult to fabricate at $x \geq 2$ (see below for details and Figure S7). The CNT content in the Ag_xSe/CNT films was fixed at 0.9 wt % (if not otherwise specified), which was identified to be the minimum loading required to produce flexible freestanding films (Figure S8).

The phase structure of the films was characterized using X-ray diffraction (XRD, Figure 2A). For all samples, the dominant diffraction peaks can be indexed to the β-Ag_2Se phase (PDF #24-1041). Notably, the phase composition is highly sensitive to the Ag/Se feeding ratio. For samples with lower Ag content (x = 1.0, 1.2, 1.4, and 1.8), additional diffraction peaks corresponding to elemental Se are observed alongside the Ag_2Se phase. The intensity of these Se peaks gradually decreases with increasing x and nearly disappears at x = 1.8 (Table S5). This trend indicates that when the Ag feeding ratio is below the stoichiometric requirement for Ag_2Se formation ($x < 1.8$), the reaction remains incomplete due to kinetic limitations associated with Ag diffusion into the Se nanowires, resulting in a two-phase composite of Ag_2Se and residual Se. Accordingly, the notation "Ag_xSe" used in this work refers to the nominal feeding ratio; the resulting products consist of Ag_2Se/Se mixtures for $x < 1.8$ and predominantly single-phase Ag_2Se at x = 1.8. As the Ag/Se molar ratio increases, the intensity of the (002) diffraction peak in the Ag_xSe/CNT composite films initially rises and subsequently declines, whereas the (013) diffraction peak exhibits the opposite trend, decreases at first and then increases. In symmetric θ-2θ XRD measurements, only lattice planes parallel to the film surface are detected. Therefore, enhanced intensity of the (002) or (013) reflection indicates a preferred orientation with these planes aligned parallel to the film plane. As thermoelectric properties are measured along the in-plane direction, charge transport occurs predominantly within these crystallographic planes. The orientation factor analysis reveals that at x = 1.8, F (013) increases to 0.27, surpassing F (002) as the dominant orientation, which favors enhanced carrier mobility and electrical conductivity (Figure 2B; Note S3). Elemental compositions and oxidation states of $Ag_{1.8}Se$/CNT and $Ag_{1.8}Se$ were further analyzed (Figures 2C and S9). The enhanced C 1*s* intensity observed in $Ag_{1.8}Se$/CNT relative to $Ag_{1.8}Se$ supports the successful integration of $Ag_{1.8}Se$ and CNT. The binding energy positions of Se $3d_{5/2}$ and Se $3d_{3/2}$ confirm the -2-oxidation state of Se, characteristic of metal-selenide bonding. The binding energy of Ag 3*d* in $Ag_{1.8}Se$/CNT composites matches that of pure $Ag_{1.8}Se$, indicating that the incorporation of CNT does not alter the chemical environment of the matrix (Figures S9C and S10). The high-resolution C 1*s* spectrum (Figure S9D) indicates that carbon is predominantly present as C–C bonds, with a minor contribution from C–O–C species, suggesting slight surface oxidation of the CNTs.

For flexible, freestanding thermoelectric films, achieving a uniform force-bearing morphology is critical, particularly at low CNT loading. This requires well-dispersed components, controlled by both the Ag/Se ratio and the choice of solvent. As illustrated in Figures 2D and S7, when $x \geq 2$ (such as 2.2), $Ag_{2.2}Se$ exhibits poor dispersibility in both EtOH and DMF, resulting in strong adhesion of the film to the substrate and ineffective co-dispersion with CNTs. As evidenced by the contact-angle and X-ray photoelectron spectroscopy (XPS) analyses (Figure S11), excess Ag increases the surface energy and alters the surface chemical states, thereby weakening solvent stabilization and promoting agglomeration (Figures 2E and S12). Reducing x to 1.8 markedly improves the dispersion of $Ag_{1.8}Se$ in DMF, although partial agglomeration still occurs in EtOH. In EtOH, adding CNTs further disrupts dispersion, causing film fracturing during peeling from the nylon substrate. This behavior is attributed to the limited dispersion capability of EtOH for both $Ag_{1.8}Se$ and CNT, where van der Waals interactions among CNT promote mutual aggregation, thereby intensifying the agglomeration phenomenon. In contrast, the higher polarity and strong coordination of DMF enable uniform dispersion of $Ag_{1.8}Se$ and CNTs, producing flexible composite films that can be easily peeled from the substrate. Scanning electron microscopy (SEM) of the as-prepared vacuum-filtrated $Ag_{1.8}Se$/CNT films further illustrates this effect. EtOH-dispersed films display loose, non-uniform porous structures, arising from inadequate dispersion that promotes particle agglomeration. The formation of large clusters impedes close packing during vacuum filtration, leading to structural heterogeneity (Figures 2F, S13, and S14). DMF-dispersed films exhibit a more uniform morphology than those obtained with EtOH (Figures 2G, S13, and S14), owing to the superior dispersing ability of DMF, which ensures homogeneous distribution of CNT and $Ag_{1.8}Se$ and promotes the formation of a densely interconnected, continuous network after vacuum filtration. We further

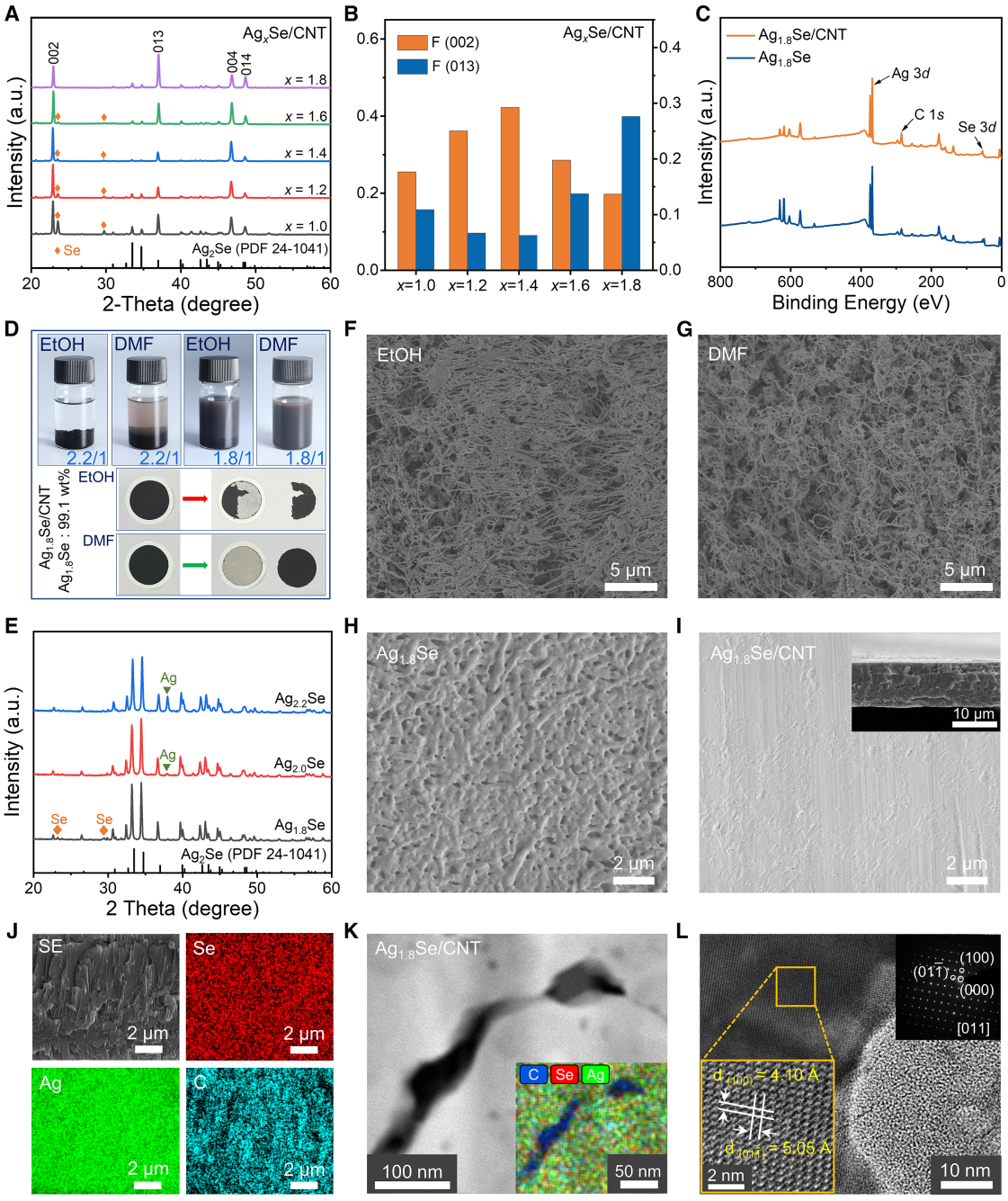

Figure 2. Phase, structure, and composition analysis of Ag_xSe/CNT films

(A) XRD patterns of Ag_xSe/CNT films prepared by hot pressing. Elemental Se is indicated by rhombus symbols.

(B) Orientation factors F (002) and F (013) of Ag_xSe/CNT films.

(C) X-ray photoelectron spectroscopy (XPS) full spectra for $Ag_{1.8}Se$/CNT and $Ag_{1.8}Se$ films.

(D) Images of Ag_xSe and CNT dispersions with different Ag/Se molar ratios in EtOH and DMF after ultrasonic treatment for 1 h (top) and corresponding $Ag_{1.8}Se$/CNT films peeled off nylon substrates (bottom).

(E) XRD patterns of $Ag_{2.2}Se$, $Ag_{2.0}Se$, and $Ag_{1.8}Se$ nanowires.

(F and G) Cross-sectional SEM images of $Ag_{1.8}Se$/CNT films prepared using EtOH (F) and DMF (G) dispersions.

(H and I) Surface SEM images of $Ag_{1.8}Se$ (H) and $Ag_{1.8}Se$/CNT (I) films after hot pressing. Inset: SEM cross-section morphology of $Ag_{1.8}Se$/CNT film.

(J) Secondary electron (SE) cross-sectional SEM image of $Ag_{1.8}Se$/CNT film and the corresponding EDS maps of Se, Ag, and C.

(K) HAADF-STEM image of the cross-section of $Ag_{1.8}Se$/CNT film and corresponding EDS elemental mapping.

(L) HRTEM image of the $Ag_{1.8}Se$/CNT film, with the insets showing the corresponding enlarged image and the SAED pattern along the [011] direction.

Please cite this article in press as: Li et al., Flexible freestanding Ag_2Se thermoelectric films with high performance for sap flow monitoring, Joule (2026), https://doi.org/10.1016/j.joule.2026.102487

investigated the morphologies of $Ag_{1.8}Se$/CNT films after hot pressing. Compared with the hot-pressed $Ag_{1.8}Se$ films (Figures 2H and S15), the hot-pressed $Ag_{1.8}Se$/CNT films exhibit reduced porosity and enhanced density (Figures 2I and S16). This improvement is attributed to the CNT network, which enhances interparticle contact and facilitates effective filling between $Ag_{1.8}Se$ nanowires.

To assess the distribution of CNTs within the hot-pressed film, energy-dispersive X-ray spectroscopy (EDS) mapping was investigated (Figure 2J). Ag, Se, and C mapping confirm uniform dispersion of CNTs with $Ag_{1.8}Se$ (Figure S17), which is further supported by the SEM image of the fractured sample obtained at room temperature (Figure S18). Additionally, the cross-sectional and surface EDS spectra reveal Ag/Se atomic ratios of 2.0183:1 and 1.9948:1, respectively (Figures S17 and S19). This deviation from the initial feed ratio (1.8:1) is attributed to the volatilization of Se during the hot-pressing process. To further elucidate the microstructure of the $Ag_{1.8}Se$/CNT composite, the samples were systematically characterized by transmission electron microscopy (TEM). High-angle annular dark-field scanning TEM (HAADF-STEM) images show close contact between amorphous and crystalline regions, with CNTs occupying the amorphous phase and $Ag_{1.8}Se$ the crystalline phase (Figures 2K and S20), which is further confirmed by EDS elemental mapping analysis. Additionally, high-resolution TEM (HRTEM) images of $Ag_{1.8}Se$ near CNTs reveal well-defined lattice fringes with spacings of 4.10 and 5.05 Å, corresponding to the (100) and (01$\bar{1}$) planes, respectively (Figure 2L). Selected area electron diffraction (SAED) patterns further confirm alignment along the [011] zone axis, thereby verifying the crystal structure of the region.

Thermoelectric properties and flexibility

To investigate the thermoelectric performance of Ag_xSe/CNT films, measurements of σ, S, and PF were conducted at 298 K along the in-plane direction. The dependence of thermoelectric properties on the Ag/Se molar ratio is presented in Figures 3A and 3B. With an increasing Ag/Se ratio, σ rises markedly, whereas S initially shows a slight decrease followed by an increase, resulting in an overall improvement in PF. Notably, $Ag_{1.8}Se$/CNT films achieve a maximum σ of 836.7 ± 47.0 S cm^{-1}, corresponding to a maximum PF of 16.8 ± 1.4 μW cm^{-1} K^{-2}. The role of CNT content in determining the thermoelectrical performance was further examined. At loadings above 0.9 wt %, the PF of Ag_xSe/CNT films declines sharply, demonstrating that excess CNT incorporation degrades thermoelectric performance (Figure S21).

To elucidate the origin of the variations of σ, S, and PF with Ag/Se ratio, Hall effect measurements were performed to determine the carrier concentration (n_H) and carrier mobility (μ_H). As shown in Figure 3C, n_H initially increases and then decreases with increasing Ag/Se ratio, confirming the variation in S. This behavior is attributed to the phase transition from a mixed Ag_2Se and Se system to a single-phase Ag_2Se, where the Se diffraction peak gradually disappears and eventually vanishes as the Ag/Se ratio increases, which is further corroborated by EDS analysis (Table S5). The EDS results show that the actual Ag/Se atomic ratio increases progressively with the nominal composition, reaching ~1.995 for the $Ag_{1.8}Se$/CNT film, corresponding to nearly stoichiometric Ag_2Se. In contrast, μ_H increases steadily as the Ag/Se ratio rises (reduction in high-resistance phase Se), reaching an exceptional value of 1,634 cm^2 v^{-1} s^{-1} at room temperature for the $Ag_{1.8}Se$/CNT film. This remarkable μ_H arises from a single Ag_2Se phase combined with the incorporation of CNTs, which exhibit high intrinsic mobility and form a continuous conductive network with $Ag_{1.8}Se$ nanowires, thereby strengthening inter-nanowire connectivity and enabling efficient carrier transport. The synergy between high μ_H and moderate n_H ensures enhanced σ while maintaining a sufficiently high S, thereby contributing to the excellent PF of the composite film. It is worth noting that the monotonic increase in μ_H and PF with Ag/Se ratio, in contrast to the non-monotonic evolution of the (002) or (013) orientation, suggests that the enhanced μ_H and PF are predominantly governed by the optimization of the Ag_2Se stoichiometry, rather than by the orientation change.

The temperature-dependent performance of the $Ag_{1.8}Se$/CNT film was analyzed over the range of 300–380 K. As shown in Figure 3D, σ increases while absolute S decreases with temperature, yielding a maximum PF of 20.9 μW cm^{-1} K^{-2} at 380 K. To assess the practical applicability of the $Ag_{1.8}Se$/CNT composite films, we examined their long-term stability and mechanical flexibility. Stability tests over 15 days show negligible changes in σ and S, confirming excellent performance stability (Figures 3E and S22). Mechanical flexibility was analyzed by measuring the normalized resistance at different bending radii. As demonstrated in Figures 3F and S23, the Ag_xSe/CNT films display superior mechanical flexibility. In particular, the σ of the $Ag_{1.8}Se$/CNT film decreased by less than 3% relative to its initial value after 1,000 bending cycles at a bending radius of 1 mm, demonstrating excellent durability for flexible thermoelectric applications. Moreover, after 20,000 cyclic bending tests at a radius of 2 mm, the thermoelectric performance remains stable, with σ, S, and PF retaining over 94%, 101%, and 95% of their initial values, respectively (Figures 3G and S24). Compared with previously reported flexible freestanding materials, the $Ag_{1.8}Se$/CNT films exhibit highly competitive flexibility (Figure 3H; Table S2).[19,25–33] Additionally, to evaluate practical durability under real-world conditions, we further investigated the material's performance under multi-axis bending, twisting, and coupled thermo-mechanical loading. The results demonstrate excellent stability of the material properties under these conditions (Figure S25).

Furthermore, the influence of film thickness on thermoelectric performance and flexibility was characterized (Figures S26 and S27). Decreasing the film thickness enhances σ, S, and PF, owing to the larger grain size and denser structure that make the hot-pressed films more similar to the properties of two-dimensional materials. The variation in flexibility stems from the cubic relationship between bending stiffness and thickness, which inherently makes thinner films more flexible. When reduced to below 10 μm, the films become difficult to peel from the nylon substrate owing to insufficient mechanical strength. Thus, a thickness of ~10 μm represents the optimal compromise between thermoelectric performance and flexibility.

Overall, these observations underscore three key requirements for achieving an optimal balance between high thermoelectric efficiency and mechanical flexibility: (1) achieving a

Please cite this article in press as: Li et al., Flexible freestanding Ag_2Se thermoelectric films with high performance for sap flow monitoring, Joule (2026), https://doi.org/10.1016/j.joule.2026.102487

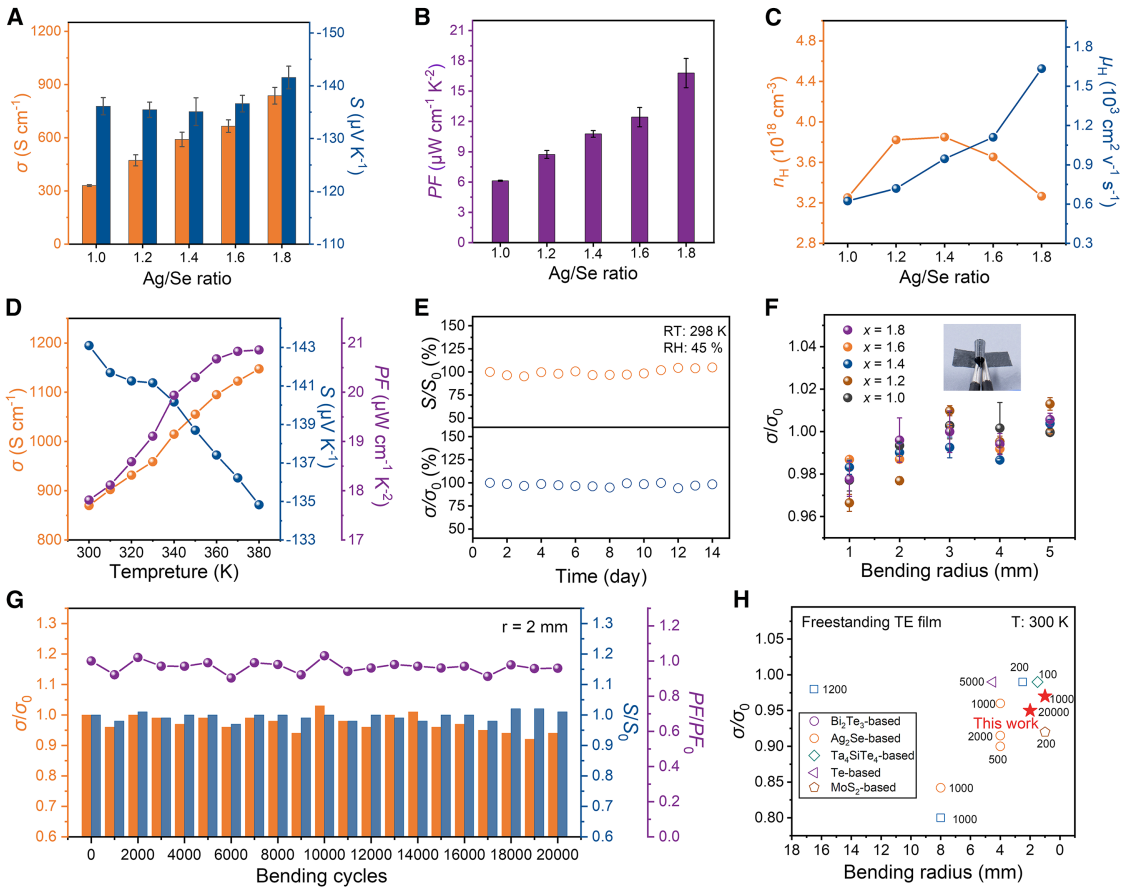

Figure 3. TE performance and flexibility of Ag_xSe/CNT films

(A and B) Room-temperature σ, and S (A) of $Ag_{1.8}Se$/CNT films with different Ag/Se molar ratios and their corresponding PF (B). The error bars represent three independent measurements.

(C) Room-temperature n_H, and μ_H of $Ag_{1.8}Se$/CNT film with varying Ag/Se molar ratios.

(D) TE properties of $Ag_{1.8}$/CNT film between 300 and 380 K.

(E) Variations of Seebeck coefficient (S/S_0) and electrical conductivity (σ/σ_0) of $Ag_{1.8}Se$/CNT film at 298 K and 45% RH over 15 days.

(F) Conductivity changes (σ/σ_0) of Ag_xSe/CNT films under different bending radii over 1,000 cycles. The error bars represent three independent measurements.

(G) TE property variations of $Ag_{1.8}Se$/CNT film at a 2-mm bending radius after 20,000 bending cycles.

(H) Relative conductivity (σ/σ_0) of freestanding TE films as a function of bending radius after different numbers of bending cycles (with data values indicated near the corresponding points).

high Ag/Se ratio while avoiding nanowires agglomeration, (2) ensuring uniform distribution of all components to facilitate the formation of abundant and stable interfacial contacts between them, and (3) minimizing the CNT filler concentration and film thickness without compromising the integrity of the freestanding structure.

High-performance recyclable thermoelectric device

Leveraging the properties-optimized $Ag_{1.8}Se$/CNT films, we constructed flexible thermoelectric devices to assess their potential utilities for sensing and power generation. We first fabricated a thermoelectric sensor comprising a single thermoelectric leg. The thermoelectric sensor exhibits a strong linear relationship between the output voltage (V) and the ΔT, with a slope of 142.24 μV/K corresponding to the S of the film (Figure 4A). At a fixed ΔT, the device provides a stable V output, confirming reliable temperature sensing (Figure 4B). Additionally, when ΔT is introduced through cooling, the device maintains similar performance, demonstrating good usage stability (Figure S28). Notably, under proportion integration differentiation (PID)-controlled temperature regulation, the device delivered a V of 4.2 μV at an ultra-small ΔT of 0.027 K (Figure 4C), highlighting its remarkable sensitivity and suitability for high-precision temperature sensing under minimal thermal gradients.

To further evaluate the potential for power generation, we fabricated an F-TEG comprising five thermoelectric legs connected in series (inset, Figure 4D). For this study, the F-TEG was integrated with a soft, comfortable, and biodegradable PLA film to demonstrate its recyclability and favorable utility for bio-interfaces. With this device design, we systematically studied its output performance.

Please cite this article in press as: Li et al., Flexible freestanding Ag_2Se thermoelectric films with high performance for sap flow monitoring, Joule (2026), https://doi.org/10.1016/j.joule.2026.102487

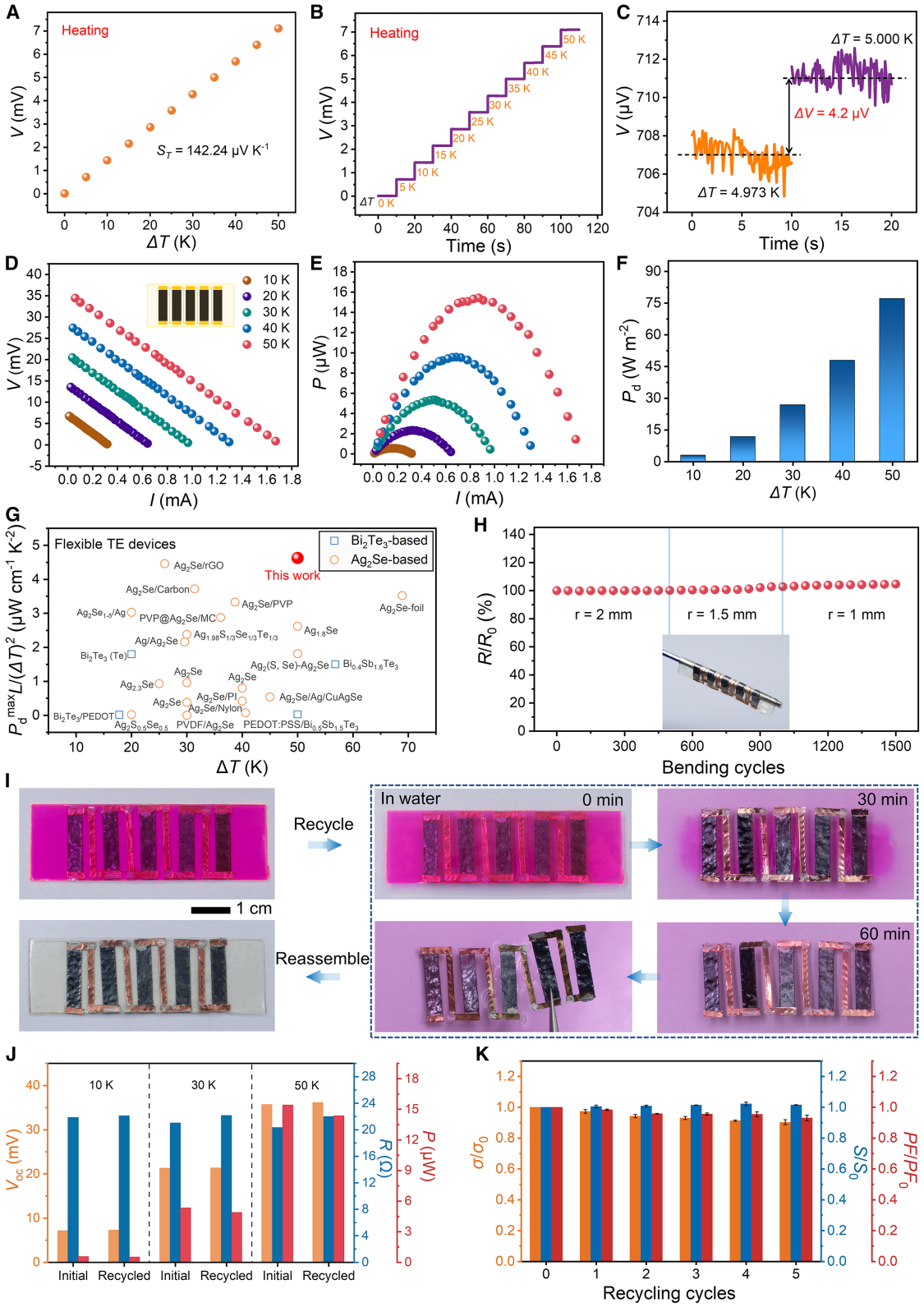

(legend on next page)

Please cite this article in press as: Li et al., Flexible freestanding Ag_2Se thermoelectric films with high performance for sap flow monitoring, Joule (2026), https://doi.org/10.1016/j.joule.2026.102487

The open-circuit voltage (V_{oc}) of the generator increases linearly with rising ΔT, reaching 35.65 mV at a ΔT of 50 K, in close agreement with the theoretical prediction (Figure S29A). The actual output performance of a thermoelectric generator under a fixed ΔT can be evaluated by measuring the V, the loading current (I), and the resulting P ($P = VI$) when connected to different external load resistors in series. As shown in Figures 4D and 4E, the V decreases proportionally with the I, while the P demonstrates a parabolic dependence on I. Moreover, both V and I increased with rising ΔT. At a ΔT of 50 K, the generator can deliver a maximum P of 15.4 μW at an external load resistance of 20 Ω (Figures S29B and S29C). For comparative evaluation of device performance, the power density (P_d) and the normalized P_d were calculated. As shown in Figure 4F, the device achieves a P_d of 77.14 W m^{-2} at a ΔT of 50 K. Moreover, the normalized P_d exhibits a slight increase with rising ΔT (Figure S30, which can be attributed to a gradual reduction in device resistance at higher ΔT. The maximum normalized P_d reaches 4.63 μW cm^{-1} K^{-2}, offering a marked advantage over previously reported flexible thermoelectric devices (Figure 4G; Table S6).[5,16,17,23,26,29–33,39,44–55] This superior performance is primarily attributed to the high PF of the $Ag_{1.8}Se$/CNT composite and the low interface resistance of the device.

We then characterized the flexibility and recyclability of the device. The device was subjected to repeated mechanical bending with different radii. As illustrated in Figure 4H, the device exhibits a resistance increase of less than 7% after 500 bending cycles, confirming its excellent mechanical flexibility and structural stability. In addition, the recyclability of the device was evaluated through water-based testing. After 60 min of immersion, the PLA film is fully degraded, thereby releasing the F-TEG device from the matrix (Figures 4I and S31). After retrieval from the solution, the device remains structurally intact and is suitable for reuse. The PLA solution can be recovered and reprocessed into films, exhibiting negligible changes in both the structures and mechanical properties before and after recycling (Figures S32 and S33). Using these recycled components, F-TEG devices were remanufactured, and their output performance as well as thermoelectrical properties were subsequently evaluated (Figures 4J and 4K). To provide a more quantitative understanding of the recycling process, we further investigated the evolution of material properties. As shown in Figure S34, the morphology and thickness of the films remain virtually unchanged after multiple recycling cycles. However, while μ_H is largely maintained, the n_H gradually decreases with cycling, which accounts for the observed slight reduction in σ and the corresponding increase in S. Notably, the PF degradation rate remains below 7% even after 5 cycles. This also explains why recycled devices exhibit an increased V_{oc} and internal resistance, along with a reduced P (<7%), compared with initial devices. Furthermore, the entire recycling loop—for both the device and the PLA substrate—employs pure water as the sole solvent (Figure S32), relying exclusively on dissolution and evaporation without any toxic organic additives. This protocol effectively avoids secondary chemical pollution, ensuring high sustainability and minimal environmental impact. These results highlight the substantial potential of our $Ag_{1.8}Se$/CNT-based flexible devices for sustainable power generation applications.

Applications for sap flow monitoring

Sap flow functions as the "pulse of life" for plants. Precise and continuous monitoring of sap movement is crucial for understanding plant water status, diagnosing health issues, and enabling precision irrigation in smart farming. Furthermore, high-quality sap flow data provide essential input for ecological hydrology, watershed modeling, and climate-change-related carbon-water coupling studies. However, commercial sap flow monitoring methods, such as thermal diffusion probes and thermal balance techniques, often rely on rigid sensor components that can cause plant tissue damage during installation and often fail to maintain stable performance as plants grow or undergo environmental fluctuations.

In contrast, the flexible $Ag_{1.8}Se$/CNT-based thermoelectric devices developed here offer a mechanically compliant and tissue-friendly alternative. Of particular significance, their highly sensitive sensing capabilities, robust power output, and excellent flexibility enable reliable operation under the subtle thermal gradients associated with plant transpiration. In addition, the $Ag_{1.8}Se$/CNT films display favorable biocompatibility (Figure S35), and encapsulation with biodegradable PLA layers[56] further ensures environmental safety and stable integration with biological tissues. Leveraging these advantages, we validate the feasibility of using these devices as multifunctional bio-interfaces capable of simultaneously sensing sap flow and harvesting energy through a proof-of-concept demonstration (Figure 5A).

Figure 5B describes the working mechanism of the self-powered wearable plant device within the monitoring system. During heater operation (active excitation source), sap flow generates a ΔT across the sensor ends, producing a V that is conditioned and transmitted to the microcontroller unit (MCU) for processing to

Figure 4. Performance, stability, and recyclability of $Ag_{1.8}Se$/CNT devices

(A) Dependence of output voltage (V) of a single $Ag_{1.8}Se$/CNT device on temperature differences (ΔT).

(B) Stable and continuous V output of a single $Ag_{1.8}Se$/CNT device as a function of time.

(C) High-sensitive response of a single $Ag_{1.8}Se$/CNT device to a small temperature change (ΔT = 0.027 K).

(D and E) Output voltages (D) and powers (P) (E) at different ΔT for the five series-connected devices as a function of output current (I).

(F) P_d ($P_d = P/NWH$, where N denotes the number of TE legs, W is the leg width, and H is the leg thickness) of the device at different ΔT.

(G) Comparison of the normalized power density ($P_dL/(\Delta T)^2$, where L represents the effective length of the TE leg excluding the electrode) at maximum P versus ΔT of flexible TE devices, as reported in previous studies and this work.

(H) Variation in device resistance after continuous bending under different bending radii.

(I) The water-based recycling and reassembling of the TE devices encapsulated with PLA films. For visualization of the recycling process, the PLA film was stained with Rhodamine B.

(J) Comparison of initial and recycled V, R, and P values of the device.

(K) Comparison of TE properties of the initial and recycled $Ag_{1.8}Se$/CNT films. The error bars represent three independent measurements.

Please cite this article in press as: Li et al., Flexible freestanding Ag_2Se thermoelectric films with high performance for sap flow monitoring, Joule (2026), https://doi.org/10.1016/j.joule.2026.102487

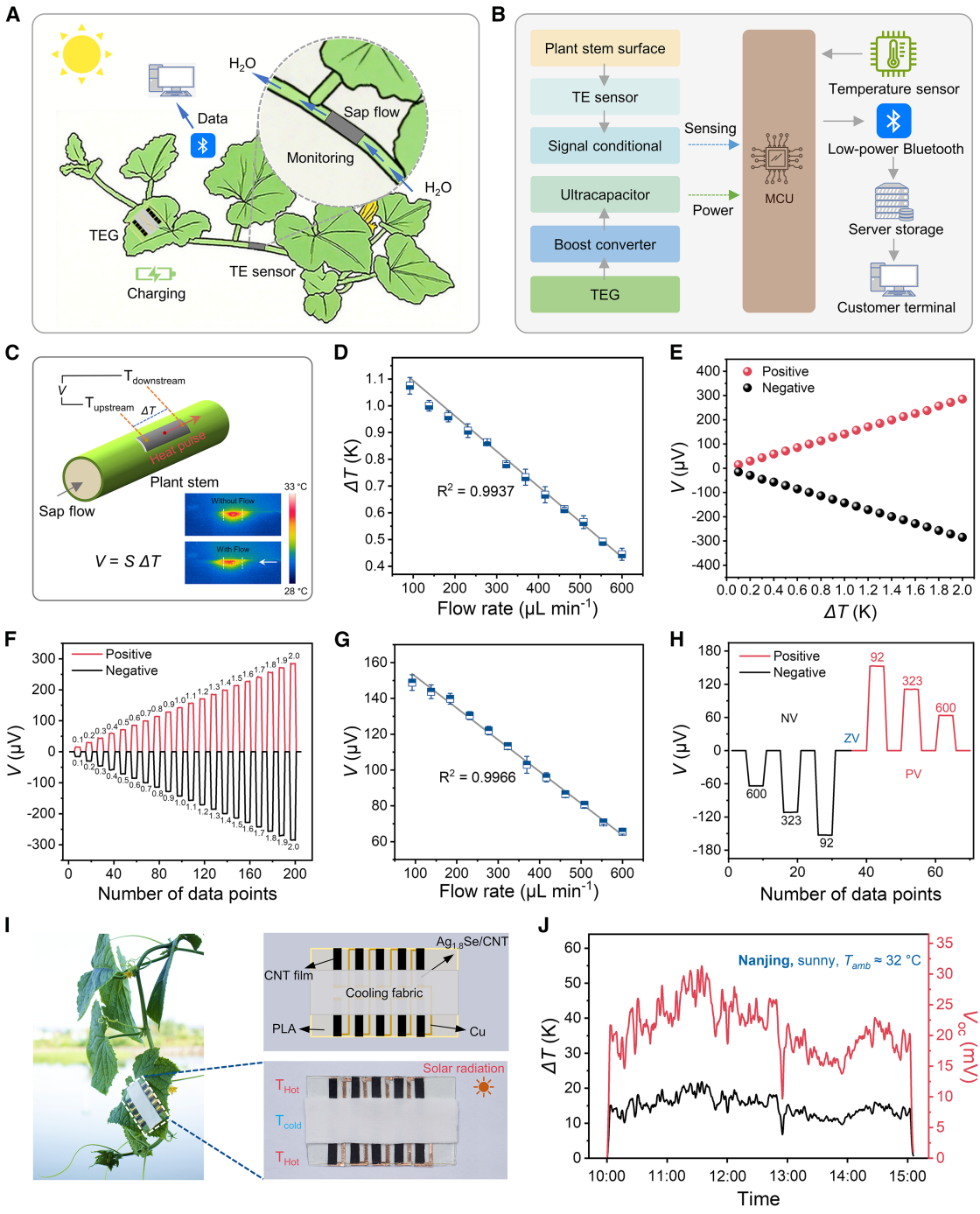

Figure 5. Utilities of $Ag_{1.8}Se$/CNT devices for plant sap flow monitoring

(A) Schematic diagram of a TE sensing device for plant sap flow monitoring and a generator (TEG) for power supply.

(B) Operating principles of the plant sap flow monitoring system.

(C) Schematic of the TE sensor for plant sap flow monitoring, with the inset showing upstream and downstream spatial temperature distributions under fixed heating, both with and without sap flow.

(D) Upstream and downstream ΔT as a function of sap flow rate (heating temperature: 34°C). The error bars represent three independent measurements.

(E) Dependence of V of the TE sensor on ΔT.

(F) Continuous V output under different ΔT.

(legend continued on next page)

Please cite this article in press as: Li et al., Flexible freestanding Ag_2Se thermoelectric films with high performance for sap flow monitoring, Joule (2026), https://doi.org/10.1016/j.joule.2026.102487

quantify the sap flow rate. The acquired data are then transmitted to a remote server via a Bluetooth module, enabling real-time monitoring through terminal devices. Meanwhile, the F-TEG harvests electrical energy by exploiting the ΔT caused by solar radiation. The harvested energy is regulated by a boost circuit and stored in a supercapacitor, providing a stable, continuous power supply to the MCU and the connected signal conditioning circuit.

Figure 5C illustrates the operating mechanism of the sensor, where activating the heating plate causes a rapid increase in local temperature (Figure S36). When simulating sap flow occurs, convective heat transfer along the flow direction induces anisotropic heat propagation within the plant stem, thereby generating a ΔT across the sensor ends (Note S4). Infrared imaging (inset, Figure 5C) shows the anisotropic temperature distribution under conditions with and without sap flow, serving as an indicator of flow direction and rate. Measurements under varying simulated flow rates demonstrate that the ΔT across the sensor exhibits a clear linear relationship with flow rate (Figures 5D and S37). Meanwhile, because of the strong linear relationship between V and ΔT, changes in V can be directly used to monitor ΔT, even under a small ΔT (<2 K, Figures 5E and 5F). Notably, the polarity of V directly reflects the direction of ΔT, with positive and negative gradients producing corresponding positive and negative voltages. Thus, a correlation between V and flow rate can be established, demonstrating a strong linear relationship (Figure 5G). Moreover, the V response (positive or negative) allows for direct determination of the sap flow direction (Figure 5H). Additionally, the excellent voltage stability across varying ΔT and flow rates further confirms the reliability of this approach for sap flow monitoring (Figures 5F and 5H). Compared with other time-based detection methods, this approach provides higher efficiency and simpler operation.[57,58]

By integrating an F-TEG onto a plant leaf, we demonstrate its capability to power the sap flow monitoring system. In this scenario, the ΔT induced by solar radiation can be harnessed to generate electricity. Specifically, we designed a device consisting of 10 series-connected thermoelectric legs, with CNT films and Al_2O_3-doped silk fabric (Figure S38) serving as photothermal conversion and radiative cooling layers, respectively.[59] This configuration establishes a ΔT across the thermoelectric legs (Figure 5I). Outdoor experiments demonstrate that a maximum ΔT of 21.9 K can be achieved during daytime operation, resulting in a V_{oc} of 31.3 mV (Figure 5J).

Overall, through a proof-of-concept demonstration, we show that integrating thermoelectric sensing with energy-harvesting devices enables simultaneous sap flow monitoring and on-site power generation under controlled conditions. By strategically optimizing monitoring intervals, implementing dormancy-activation schemes for system components, and compensating for environmental temperature fluctuations, this approach establishes a robust foundation for long-term, stable monitoring and reliable data transmission in practical plant sap flow applications.

DISCUSSION

In summary, we have successfully developed the facile fabrication of freestanding $Ag_{1.8}Se$/CNT thermoelectric composite films that overcome the long-standing trade-offs among mechanical flexibility, thermoelectric performance, power output, and sustainable manufacturing, through refined structural design. With an ultralow CNT content of 0.9 wt %, the composite achieves an exceptional PF of 20.9 $\mu W\ cm^{-1}\ K^{-2}$ at 380 K, outstanding flexibility enduring 20,000 bending cycles at a 2-mm radius, and facile fabrication under a mild processing temperature of 413 K. The resulting flexible generator exhibits a compelling P of 15.4 μW and a normalized P_d of 4.63 $\mu W\ cm^{-1}\ K^{-2}$ at a ΔT of 50 K. The remarkable performance of the composite film and the derived devices stems mainly from the optimized Ag/Se molar ratio and the homogeneous co-dispersion of $Ag_{1.8}Se$ and CNTs within the matrix, and it is anticipated to be further enhanced through the involvement of microstructural optimization strategies, such as orientation engineering. The assembled device combines high-sensitivity sensing, a continuous and stable self-powered energy supply, and adaptability to diverse surfaces, expanding its utility to flexible electronics, wearable technologies, and non-planar thermal management well beyond the applications demonstrated here. In particular, the excellent biocompatibility of the components creates opportunities for bio-integrated thermoelectric systems operating at the biology-technology interface. Moreover, the capacity to conform to various substrates presents a promising pathway toward multifunctional devices with improved versatility and adaptability. Notably, the structural design strategy presented here is not material-specific and can be applied to other inorganic thermoelectric systems (Figure S39), paving the way for high-performance, flexible, and sustainable electronics in next-generation wearable and IoT technologies.

METHODS

Detailed methods can be found in the supplemental information.

RESOURCE AVAILABILITY

Lead contact

Requests for further information and resources should be directed to and will be fulfilled by the lead contact, Yu Wang (yuwang87@nju.edu.cn).

Materials availability

All materials generated in this study will be made available by the lead contact upon reasonable request.

(G) Correlation between V of the TE sensor and plant sap flow rate. The error bars represent three independent measurements.
(H) Relationship between TE sensor V, plant sap flow rate, and flow direction.
(I) A TEG attached to a plant leaf, along with its detailed structural organization, including both a schematic illustration and the corresponding photograph.
(J) Measured ΔT and V of the TEG under daytime exposure.

Data and code availability

The data and code that support the conclusions of this study are available from the lead contact upon reasonable request.

ACKNOWLEDGMENTS

This work was supported by the National Key R&D Program of China (no. 2022YFA1203700 [Y.W.], no. 2022YFA1405000 [Y.-Q.L.], and no. 2021YFA1202000 [Y.W.]); the National Natural Science Foundation of China (no. 62175102 [Y.W.] and no. T2488302 [Y.-Q.L.]); the Natural Science Foundation of Jiangsu Province (no. BK20243067 [Y.-Q.L.]); and the Fundamental Research Funds for the Central Universities (Y.W.).

AUTHOR CONTRIBUTIONS

Y.W. and G.L. conceived the idea and designed the research. G.L. synthesized and characterized the thermoelectric films and devices. X.-R.G. participated in the preparation and characterization of the PLA film. T.W. and J.W. assisted in material morphology characterization. All authors contributed to the data analysis. G.L., Y.W., G.C., and Y.-Q.L. wrote and revised the manuscript. Y.W., G.C., and Y.-Q.L. supervised the research. All authors approved the final version of the manuscript.

DECLARATION OF INTERESTS

The authors declare no competing interests.

DECLARATION OF GENERATIVE AI AND AI-ASSISTED TECHNOLOGIES IN THE WRITING PROCESS

During the preparation of this work, the authors used ChatGPT (OpenAI) to improve the readability and language of the manuscript. After using this tool, the authors reviewed and edited the content as needed and take full responsibility for the content of the publication.

SUPPLEMENTAL INFORMATION

Supplemental information can be found online at https://doi.org/10.1016/j.joule.2026.102487.

Received: December 23, 2025
Revised: April 1, 2026
Accepted: April 23, 2026

REFERENCES

1. Xiao, Y., and Zhao, L.D. (2020). Seeking new, highly effective thermoelectrics. Science *367*, 1196–1197. https://doi.org/10.1126/science.aaz9426.
2. Tang, W., Sun, Q., and Wang, Z.L. (2023). Self-powered sensing in wearable electronics-A paradigm shift technology. Chem. Rev. *123*, 12105–12134. https://doi.org/10.1021/acs.chemrev.3c00305.
3. Wan, C., Gu, X., Dang, F., Itoh, T., Wang, Y., Sasaki, H., Kondo, M., Koga, K., Yabuki, K., Snyder, G.J., et al. (2015). Flexible n-type thermoelectric materials by organic intercalation of layered transition metal dichalcogenide TiS_2. Nat. Mater. *14*, 622–627. https://doi.org/10.1038/nmat4251.
4. Yang, Q., Yang, S., Qiu, P., Peng, L., Wei, T.R., Zhang, Z., Shi, X., and Chen, L. (2022). Flexible thermoelectrics based on ductile semiconductors. Science *377*, 854–858. https://doi.org/10.1126/science.abq0682.
5. Chen, W., Shi, X.L., Li, M., Liu, T., Mao, Y., Liu, Q., Dargusch, M., Zou, J., Lu, G.Q.M., and Chen, Z.G. (2024). Nanobinders advance screen-printed flexible thermoelectrics. Science *386*, 1265–1271. https://doi.org/10.1126/science.ads5868.
6. Mao, J., Liu, Z., Zhou, J., Zhu, H., Zhang, Q., Chen, G., and Ren, Z. (2018). Advances in thermoelectrics. Adv. Phys. *67*, 69–147. https://doi.org/10.1080/00018732.2018.1551715.
7. Cao, T., Shi, X.L., and Chen, Z.G. (2023). Advances in the design and assembly of flexible thermoelectric device. Prog. Mater. Sci. *131*, 101003. https://doi.org/10.1016/j.pmatsci.2022.101003.
8. Zheng, Z.H., Shi, X.L., Ao, D.W., Liu, W.D., Li, M., Kou, L.Z., Chen, Y.X., Li, F., Wei, M., Liang, G.X., et al. (2023). Harvesting waste heat with flexible Bi_2Te_3 thermoelectric thin film. Nat. Sustain. *6*, 180–191. https://doi.org/10.1038/s41893-022-01003-6.
9. Lu, Y., Zhou, Y., Wang, W., Hu, M., Huang, X., Mao, D., Huang, S., Xie, L., Lin, P., Jiang, B., et al. (2023). Staggered-layer-boosted flexible Bi_2Te_3 films with high thermoelectric performance. Nat. Nanotechnol. *18*, 1281–1288. https://doi.org/10.1038/s41565-023-01457-5.
10. Li, D., Shi, X.L., Zhu, J., Cao, T., Ma, X., Li, M., Han, Z., Feng, Z., Chen, Y., Wang, J., et al. (2024). High-performance flexible p-type Ce-filled Fe_3CoSb_{12} skutterudite thin film for medium-to-high-temperature applications. Nat. Commun. *15*, 4242. https://doi.org/10.1038/s41467-024-48677-4.
11. Kim, S.J., Lee, H.E., Choi, H., Kim, Y., We, J.H., Shin, J.S., Lee, K.J., and Cho, B.J. (2016). High-performance flexible thermoelectric power generator using laser multiscanning lift-off process. ACS Nano *10*, 10851–10857. https://doi.org/10.1021/acsnano.6b05004.
12. Kim, S.J., We, J.H., and Cho, B.J. (2014). A wearable thermoelectric generator fabricated on a glass fabric. Energy Environ. Sci. *7*, 1959–1965. https://doi.org/10.1039/c4ee00242c.
13. Liang, Z., Shu, R., Xu, C., Wang, Y., Shang, H., Mao, J., and Ren, Z. (2025). Substrate-free inorganic-based films for thermoelectric applications. Adv. Mater. *37*, e2416394. https://doi.org/10.1002/adma.202416394.
14. Wu, H., Shi, X.L., Mao, Y., Li, M., Liu, W.D., Wang, D.Z., Yin, L.C., Zhu, M., Wang, Y., Duan, J., et al. (2023). Optimized thermoelectric performance and plasticity of ductile semiconductor $Ag_2S_{0.5}Se_{0.5}$ via dual-phase engineering. Adv. Energy Mater. *13*, 2302551. https://doi.org/10.1002/aenm.202302551.
15. Wu, H., Shi, X., Duan, J., Liu, Q., and Chen, Z.G. (2023). Advances in Ag_2Se-based thermoelectrics from materials to applications. Energy Environ. Sci. *16*, 1870–1906. https://doi.org/10.1039/d3ee00378g.
16. Ding, W., Shen, X., Jin, M., Hu, Y., Chen, Z., Meng, E., Luo, J., Li, W., and Pei, Y. (2024). Robust bendable thermoelectric generators enabled by elasticity strengthening. Nat. Commun. *15*, 9767. https://doi.org/10.1038/s41467-024-54084-6.
17. Wu, H., Shi, X.L., Li, M., Gao, H., Liu, W.D., Zhu, M., Yin, L.C., Wang, D.Z., Duan, J., Chen, Z.G., et al. (2025). Sandwich engineering advances ductile thermoelectrics. Adv. Mater. *37*, e2503020. https://doi.org/10.1002/adma.202503020.
18. Gao, Z., Yang, S., Ma, Y., Wei, T.R., Chen, X., Zheng, W., Qiu, P., Zeng, X., Chen, L., and Shi, X. (2025). Warm metalworking for plastic manufacturing in brittle semiconductors. Nat. Mater. *24*, 1538–1544. https://doi.org/10.1038/s41563-025-02223-9.
19. Chen, Z., Lv, H., Zhang, Q., Wang, H., and Chen, G. (2022). Construction of a cement-rebar nanoarchitecture for a solution-processed and flexible film of a Bi_2Te_3/CNT hybrid toward low thermal conductivity and high thermoelectric performance. Carbon Energy *4*, 115–128. https://doi.org/10.1002/cey2.161.
20. Jin, Q., Jiang, S., Zhao, Y., Wang, D., Qiu, J., Tang, D.M., Tan, J., Sun, D.M., Hou, P.X., Chen, X.Q., et al. (2019). Flexible layer-structured Bi_2Te_3 thermoelectric on a carbon nanotube scaffold. Nat. Mater. *18*, 62–68. https://doi.org/10.1038/s41563-018-0217-z.
21. Liu, Y.M., Shi, X.L., Wu, T., Wu, H., Mao, Y., Cao, T., Wang, D.Z., Liu, W.D., Li, M., Liu, Q., et al. (2024). Boosting thermoelectric performance of single-walled carbon nanotubes-based films through rational triple treatments. Nat. Commun. *15*, 3426. https://doi.org/10.1038/s41467-024-47417-y.

22. Wang, H., Liu, X., Zhou, Z., Wu, H., Chen, Y., Zhang, B., Wang, G., Zhou, X., and Han, G. (2022). Constructing n-type Ag_2Se/CNTs composites toward synergistically enhanced thermoelectric and mechanical performance. Acta Mater. *223*, 117502. https://doi.org/10.1016/j.actamat.2021.117502.

23. Zhang, L., Shi, X.L., Shang, H., Gu, H., Chen, W., Li, M., Huang, D., Dong, H., Wang, X., Ding, F., et al. (2025). High-performance Ag_2Se-based thermoelectrics for wearable electronics. Nat. Commun. *16*, 5002. https://doi.org/10.1038/s41467-025-60284-5.

24. Lv, W., Tang, W., Yu, P., Kainat, J., Zhou, Z., Lan, J.L., Yang, X., and Lin, Y.H. (2025). Polymorphic interface engineering for high-performance Ag_2Se-based flexible thermoelectric device. J. Colloid Interface Sci. *699*, 138307. https://doi.org/10.1016/j.jcis.2025.138307.

25. Wang, Y., Hong, M., Liu, W.D., Shi, X.L., Xu, S.D., Sun, Q., Gao, H., Lu, S., Zou, J., and Chen, Z.G. (2020). $Bi_{0.5}Sb_{1.5}Te_3$/PEDOT: PSS-based flexible thermoelectric film and device. Chem. Eng. J. *397*, 125360. https://doi.org/10.1016/j.cej.2020.125360.

26. Zhou, H., Zhang, Z., Sun, C., Deng, H., and Fu, Q. (2020). Biomimetic approach to facilitate the high filler content in free-standing and flexible thermoelectric polymer composite films based on PVDF and Ag_2Se nanowires. ACS Appl. Mater. Interfaces *12*, 51506–51516. https://doi.org/10.1021/acsami.0c15414.

27. Xu, Q., Qu, S., Ming, C., Qiu, P., Yao, Q., Zhu, C., Wei, T.R., He, J., Shi, X., and Chen, L. (2020). Conformal organic-inorganic semiconductor composites for flexible thermoelectrics. Energy Environ. Sci. *13*, 511–518. https://doi.org/10.1039/c9ee03776d.

28. Na, Y., Kim, S., Mallem, S.P.R., Yi, S., Kim, K.T., and Park, K.-I. (2022). Energy harvesting from human body heat using highly flexible thermoelectric generator based on Bi_2Te_3 particles and polymer composite. J. Alloys Compd. *924*, 166575. https://doi.org/10.1016/j.jallcom.2022.166575.

29. Li, J., Shi, Q., Röhr, J.A., Wu, H., Wu, B., Guo, Y., Zhang, Q., Hou, C., Li, Y., and Wang, H. (2020). Flexible 3D porous MoS_2/CNTs architectures with ZT of 0.17 at room temperature for wearable thermoelectric applications. Adv. Funct. Mater. *30*, 2002508. https://doi.org/10.1002/adfm.202002508.

30. Wang, H., Lin, X., Han, G., Zhang, B., Chen, Y., Zhang, L., Lu, X., Wang, G., and Zhou, X. (2025). Flexible porous Ag_2Se films: From freestanding inorganic films to inorganic-network/organic-skeleton thermoelectric generators. Adv. Funct. Mater. *35*, 2413605. https://doi.org/10.1002/adfm.202413605.

31. Liang, L., Wang, M., Wang, X., Peng, P., Liu, Z., Chen, G., and Sun, G. (2022). Initiating a Stretchable, Compressible, and Wearable Thermoelectric Generator by a Spiral Architecture with Ternary Nanocomposites for Efficient Heat Harvesting. Adv. Funct. Mater. *32*, 2111435. https://doi.org/10.1002/adfm.202111435.

32. Sun, L., Ao, D.W., Hwang, J., Liu, Q., Cao, E.S., and Sun, B. (2024). Realizing high thermoelectric performance flexible free-standing PEDOT:PSS/$Bi_{0.5}Sb_{1.5}Te_3$ composite films for power generation. Rare Met. *43*, 5985–5993. https://doi.org/10.1007/s12598-024-02860-0.

33. Li, J., Liu, Y., Wang, Z., Chen, L., and Cai, K. (2023). Ultra-flexible self-supporting Ag_2Se/nylon composite films for wearable thermoelectric devices. Compos. B Eng. *265*, 110946. https://doi.org/10.1016/j.compositesb.2023.110946.

34. Cao, T., Shi, X.L., Hu, B., Yang, Q., Lyu, W.Y., Sun, S., Yin, L.C., Liu, Q.Y., Chen, W., Wang, X., et al. (2025). Advancing Ag_2Se thin-film thermoelectrics via selenization-driven anisotropy control. Nat. Commun. *16*, 1555. https://doi.org/10.1038/s41467-025-56671-7.

35. Hu, Q.X., Liu, W.D., Zhang, L., Gao, H., Wang, D.Z., Wu, T., Shi, X.L., Li, M., Liu, Q.F., Yang, Y.L., et al. (2024). Carrier separation boosts thermoelectric performance of flexible n-type Ag_2Se-based films. Adv. Energy Mater. *14*, 2401890. https://doi.org/10.1002/aenm.202401890.

36. Chen, Y.X., Shi, X.L., Zhang, J.Z., Nisar, M., Zha, Z.Z., Zhong, Z.N., Li, F., Liang, G.X., Luo, J.T., Li, M., et al. (2024). Deviceization of high-performance and flexible Ag_2Se films for electronic skin and servo rotation angle control. Nat. Commun. *15*, 8356. https://doi.org/10.1038/s41467-024-52680-0.

37. Li, Y., Lou, Q., Yang, J., Cai, K., Liu, Y., Lu, Y., Qiu, Y., Lu, Y., Wang, Z., Wu, M., et al. (2022). Exceptionally high power factor Ag_2Se/Se/polypyrrole composite films for flexible thermoelectric generators. Adv. Funct. Mater. *32*, 2106902. https://doi.org/10.1002/adfm.202106902.

38. Yang, D., Shi, X.L., Li, M., Nisar, M., Mansoor, A., Chen, S., Chen, Y., Li, F., Ma, H., Liang, G.X., et al. (2024). Flexible power generators by Ag_2Se thin films with record-high thermoelectric performance. Nat. Commun. *15*, 923. https://doi.org/10.1038/s41467-024-45092-7.

39. Hou, S., Liu, Y., Yin, L., Chen, C., Wu, Z., Wang, J., Luo, Y., Xue, W., Liu, X., Zhang, Q., et al. (2021). High performance wearable thermoelectric generators using Ag_2Se films with large carrier mobility. Nano Energy *87*, 106223. https://doi.org/10.1016/j.nanoen.2021.106223.

40. Hou, S., Liu, Y., Luo, Y., Wang, X., Yin, L., Sun, X., Wu, Z., Wang, J., Li, M., Chen, Z., et al. (2022). High-performance, thin-film thermoelectric generator with self-healing ability for body-heat harvesting. Cell Rep. Phys. Sci. *3*, 101146. https://doi.org/10.1016/j.xcrp.2022.101146.

41. Lei, Y., Qi, R., Chen, M., Chen, H., Xing, C., Sui, F., Gu, L., He, W., Zhang, Y., Baba, T., et al. (2022). Microstructurally tailored thin β-Ag_2Se films toward commercial flexible thermoelectrics. Adv. Mater. *34*, e2104786. https://doi.org/10.1002/adma.202104786.

42. Zheng, Z.H., Li, Y.L., Niu, J.Y., Wei, M., Zhang, D.L., Zhong, Y., Nisar, M., Abbas, A., Chen, S., Li, F., et al. (2022). Significantly (00l)-textured Ag_2Se thin films with excellent thermoelectric performance for flexible power applications. J. Mater. Chem. A *10*, 21603–21610. https://doi.org/10.1039/d2ta06356e.

43. Lu, Y., Qiu, Y., Cai, K., Li, X., Gao, M., Jiang, C., and He, J. (2020). Ultrahigh performance PEDOT/Ag_2Se/CuAgSe composite film for wearable thermoelectric power generators. Mater. Today Phys. *14*, 100223. https://doi.org/10.1016/j.mtphys.2020.100223.

44. Lu, Y., Qiu, Y., Cai, K., Ding, Y., Wang, M., Jiang, C., Yao, Q., Huang, C., Chen, L., and He, J. (2020). Correction: Ultrahigh power factor and flexible silver selenide-based composite film for thermoelectric devices. Energy Environ. Sci. *13*, 1287–1288. https://doi.org/10.1039/d0ee90012e.

45. Mao, D., Zhou, Y., Yu, Y., Wang, Y., Han, M., Meng, Q., Lu, Y., Feng, J., Kong, M., Yang, H., et al. (2024). Scalable and sustainable manufacturing of twin boundary-enhanced flexible $Bi_{0.4}Sb_{1.6}Te_3$ films with high thermoelectric performance. Joule *8*, 3313–3323. https://doi.org/10.1016/j.joule.2024.08.009.

46. Li, X., Lu, Y., Cai, K., Gao, M., Li, Y., Wang, Z., Wu, M., Wei, P., Zhao, W., Du, Y., et al. (2022). Exceptional power factor of flexible Ag/Ag_2Se thermoelectric composite films. Chem. Eng. J. *434*, 134739. https://doi.org/10.1016/j.cej.2022.134739.

47. Liang, J., Wang, T., Qiu, P., Yang, S., Ming, C., Chen, H., Song, Q., Zhao, K., Wei, T.R., Ren, D., et al. (2019). Flexible thermoelectrics: From silver chalcogenides to full-inorganic devices. Energy Environ. Sci. *12*, 2983–2990. https://doi.org/10.1039/c9ee01777a.

48. Liu, Y., Zhang, Q., Huang, A., Zhang, K., Wan, S., Chen, H., Fu, Y., Zuo, W., Wang, Y., Cao, X., et al. (2024). Fully inkjet-printed Ag_2Se flexible thermoelectric devices for sustainable power generation. Nat. Commun. *15*, 2141. https://doi.org/10.1038/s41467-024-46183-1.

49. Ding, Y., Qiu, Y., Cai, K., Yao, Q., Chen, S., Chen, L., and He, J. (2019). High performance n-type Ag_2Se film on nylon membrane for flexible thermoelectric power generator. Nat. Commun. *10*, 841. https://doi.org/10.1038/s41467-019-08835-5.

50. Chen, H., Shao, C., Huang, S., Gao, Z., Huang, H., Pan, Z., Zhao, K., Qiu, P., Wei, T.R., and Shi, X. (2024). High-entropy cubic pseudo-ternary Ag_2(S, Se, Te) materials with excellent ductility and thermoelectric performance. Adv. Energy Mater. *14*, 2303473. https://doi.org/10.1002/aenm.202303473.

51. Kumar, S., Battabyal, M., Sethupathi, K., and Satapathy, D.K. (2024). High-performance printed Ag_2Se/PI flexible thermoelectric film for

powering wearable electronics. ACS Appl. Mater. Interfaces *16*, 40848–40857. https://doi.org/10.1021/acsami.4c05537.

52. Lu, Y., Han, X., Wei, P., Liu, Y., Wang, Z., Zuo, X., Zhao, W., and Cai, K. (2024). Nanoengineering approach toward ultrahigh power factor Ag_2Se/polyvinylpyrrolidone composite film for flexible thermoelectric generator. Chem. Eng. J. *485*, 149793. https://doi.org/10.1016/j.cej.2024.149793.

53. Zhang, M., Li, J., Liu, Y., Liu, Y., Huang, C., Liu, R., Wei, P., Zhao, W., Xie, W., Weidenkaff, A., et al. (2025). Screen printing high-performance free-standing Ag_2Se/carbon composite film for flexible thermoelectric converters. Nano Energy *138*, 110836. https://doi.org/10.1016/j.nanoen.2025.110836.

54. Gao, J., Miao, L., Lai, H., Zhu, S., Peng, Y., Wang, X., Koumoto, K., and Cai, H. (2020). Thermoelectric flexible silver selenide films: Compositional and length optimization. iScience *23*, 100753. https://doi.org/10.1016/j.isci.2019.100753.

55. Qin, J., Du, Y., Meng, Q., Chen, S., Hong, M., and Ke, Q. (2025). Versatile polymer-coated Ag_2Se thermoelectric materials and devices for multi-scenario applications developed by direct-ink printing. Nat. Commun. *16*, 8497. https://doi.org/10.1038/s41467-025-63390-6.

56. Qi, Y., Xu, C., Zhang, Z., Zhang, Q., Xu, Z., Zhao, X., Zhao, Y., Cui, C., and Liu, W. (2024). Wet environment-induced adhesion and softening of coenzyme-based polymer elastic patch for treating periodontitis. Bioact. Mater. *35*, 259–273. https://doi.org/10.1016/j.bioactmat.2024.02.002.

57. Chai, Y., Chen, C., Luo, X., Zhan, S., Kim, J., Luo, J., Wang, X., Hu, Z., Ying, Y., and Liu, X. (2021). Cohabiting plant-wearable sensor in situ monitors water transport in plant. Adv. Sci. (Weinh) *8*, 2003642. https://doi.org/10.1002/advs.202003642.

58. Wang, S., Chai, Y., Sa, H., Ye, W., Wang, Q., Zou, Y., Luo, X., Xie, L., and Liu, X. (2024). Sunflower-like self-sustainable plant-wearable sensing probe. Sci. Adv. *10*, eads1136. https://doi.org/10.1126/sciadv.ads1136.

59. Zhu, B., Li, W., Zhang, Q., Li, D., Liu, X., Wang, Y., Xu, N., Wu, Z., Li, J., Li, X., et al. (2021). Subambient daytime radiative cooling textile based on nanoprocessed silk. Nat. Nanotechnol. *16*, 1342–1348. https://doi.org/10.1038/s41565-021-00987-0.

Joule, Volume *10*

Supplemental information

Flexible freestanding Ag_2Se thermoelectric films with high performance for sap flow monitoring

Gang Li (李钢), Xiang-Rui Guo (郭祥瑞), Tao Wang (汪涛), Jing Wang (王晶), Yu Wang (王瑜), Guangming Chen (陈光明), and Yan-Qing Lu (陆延青)

Supplemental Methods

Materials

SeO_2 (Maclin, 99.99%). $AgNO_3$ (Sinopharm Chemical Reagent Co., Ltd. (China), 99.8%). *β*-cyclodextrin (Energy Chemical, 99%), L-ascorbic acid (Energy Chemical, 98%). Ethylene glycol (Aladdin, 99%). N, N-dimethylformamide (Aladdin, 99.8%). CNT (Chengdu Organic Chemicals Co. Ltd., TNSAR, 95 wt%, diameters: 1-2 nm, length: 5-30 μm, Single-walled, Figure S40). All chemicals are used as prescribed.

Synthesis of Se nanowires

SeO_2 (1 g) and *β*-cyclodextrin (1 g) were dissolved in 200 mL of deionized water under stirring to obtain solution *A*. Separately, L-ascorbic acid (4 g) was dissolved in 200 mL of deionized water to obtain solution *B*. Solution *A* was then slowly added dropwise to solution *B* under continuous stirring, and the reaction was maintained for 4 hours at 298 K to yield amorphous Se. The product was collected by centrifugation after thorough washing with deionized water and ethanol, yielding a brick-red precipitate. The precipitate was subsequently dispersed in 200 mL of ethanol and stored at 298 K for 24 hours, followed by repeated washing with deionized water and ethanol, and then dried to obtain Se nanowires (Figure S41).

Synthesize Ag_xSe nanowires

A total of 150 mg of Se nanowires was dispersed in 200 mL of ethylene glycol to form a uniform suspension, which was then heated in a water bath at 313 K. Subsequently, 1.5 g of L-ascorbic acid dissolved in 20 mL of deionized water and a stoichiometric amount of $AgNO_3$ solution (n_{Ag}: $n_{Se} = x$, $x = 1.0, 1.2, 1.4, 1.6, 1.8$) prepared in 20 mL of deionized water were sequentially added to the Se suspension. After stirring for 2 hours, the resulting black product was collected by washing with deionized water and ethanol, followed by centrifugation and vacuum drying, yielding Ag_xSe nanowires.

Fabrication of freestanding Ag_xSe/CNT film

The flexible freestanding Ag_xSe/CNT film was fabricated through a combination of vacuum filtration and hot-pressing, where x represents the molar ratio of Ag to Se. A typical synthesis procedure is as follows: 99.1 mg of Ag_xSe nanoparticles and 0.9 mg of CNT were added to 20 mL of DMF and ultrasonicated in an ice bath for 10 minutes to ensure complete dispersion. Subsequently, the dispersion was subjected to vacuum filtration, and the resulting film was vacuum-dried at 60 °C for 4 hours. The Ag_xSe/CNT film was then carefully peeled from the nylon substrate. Finally, the freestanding film was hot-pressed at 140 °C under 5 MPa, with a heating rate of 5 °C/min and a holding time of 30 minutes, followed by natural cooling to room temperature.

Ag_xSe/CNT F-TEG Fabrication

The Ag_xSe/CNT flexible device was fabricated by cutting the Ag_xSe/CNT composite film into rectangular strips with dimensions of 18 mm × 4 mm × 0.01 mm (L × W × H), and then connecting them in series with rectangular copper foils (1.5 mm) and copper wires. Conductive

silver adhesive is used to connect the material to the copper foil to reduce the interfacial resistance.

Characterization: All Ag_xSe films were characterized by XRD using Cu Kα radiation to obtain their crystal structure and phase composition. SEM (Quattro S, Thermo Fisher Scientific, USA) and TEM (Tecnai F20, FEI, Netherlands) were adopted to characterize the morphology of the material, while elemental composition was determined using EDS. The TEM samples were fabricated using a FIB (Helios G4 CX DualBeam, Thermo Fisher Scientific, USA) system. The work functions of $Ag_{1.8}Se$ and CNT were tested by ultraviolet photoelectron spectroscopy (UPS, ESCLAB 250Xi, Thermo Fischer Scientific, USA). The elemental composition and chemical state of the material surface were analyzed using an XPS (K-Alpha, Thermo Fischer Scientific, USA); all XPS spectra were calibrated using the C 1*s* peak (C-C at 284.8 eV) as a reference. The FTIR spectra were recorded from an FTIR spectrometer (Invenio S, Bruker, Germany). The mechanical properties of the polysulfide diacylglycerol membrane were tested using a universal testing machine (HY-0580, Hengyi, China). The flow rate is controlled by a peristaltic pump (B10, Yanxiao, China). The temperature profile measurement or thermal image capturing was performed by an IR camera (628C, Forric, China). The reflectance of Al_2O_3-doped silk fabric was measured using a UV-Vis-IR spectrophotometer (UV 3600, Shimadzu, Japan).

Thermoelectric property and flexibility testing

The σ and S of the material at room temperature and variable temperature (300-380 K) were measured using the MRS-3RT and MRS-3 (JouleYaCht, China), respectively. The n_H and μ_H of the material at room temperature were tested by the HMS-5000 instrument. The output performance of the flexible thermoelectric generator was evaluated using a custom-built measurement system. By connecting two Peltier elements to a digital PID temperature controller (TEC215L, SenseFuture, China), the temperature can be regulated with an accuracy of ± 0.001°C. The Peltier elements heat the two ends of the material to establish a ΔT, and a Keithley 7700 data acquisition system is used to record the resulting voltage and current under this fixed temperature gradient. The flexibility of the material was evaluated by bending it around cylinders of different radii. For the 2 mm bending radius test, a cylindrical mandrel with a radius of 2 mm was used to perform cyclic bending of the samples. The thermoelectric properties were measured using an MRS-3RT system after every 1,000 bending cycles. The device resistance after bending was measured using the two-wire method with a Keithley 7700 data acquisition system.

Sap flow testing

1. **Detailed experimental setup**: An aqueous solution containing 5% glycerol was utilized to mimic the viscosity and thermal properties of natural plant sap. Peristaltic pumps are used to regulate flow rate. The heating element is a PI polyimide heating film, driven by a temperature controller (TEC215L) based on a set temperature, with a maximum rated

power of 4 W (The controller dynamically adjusts power output based on the set temperature). The heating film is positioned at the center of the stem segment, with thermoelectric patches placed symmetrically about the heating film (length: 3 cm). Wrap the sensor area with a layer of foam, then cover it with aluminum foil to minimize interference from external factors such as humidity, radiation, and wind. Wires extend from the thermoelectric patches for voltage acquisition. Thermocouples are arranged at both ends of the thermoelectric patches for real-time temperature measurement.

2. **Power budget and matching analysis:** To clarify the power-matching feasibility, the TEG array generates a continuous power of approximately 3-6 μW. To accommodate this micro-energy generation, the sensing node employs an extreme duty-cycling strategy: it wakes up to acquire and transmit sap-flow data only once per day, remaining in an ultra-low-power deep sleep mode for the remainder of the time. The continuous microwatt-level energy harvested over 24 hours is buffered in an ultracapacitor, accumulating sufficient total energy to sustain the minimal sleep current and power the brief milliwatt-level burst required for the daily wireless transmission, thereby achieving a self-sustained data link. This analysis confirms that while the heater is externally powered, the sensing and communication infrastructure is entirely self-sustaining.

3. **Scope of "self-powered":** The heater is powered by an external source, and this component constitutes an active thermal excitation rather than a self-sustaining circuit. The "self-powered" aspect refers exclusively to the data acquisition, processing, and wireless communication chain, which operates on harvested thermoelectric energy.

Supplemental Notes

Note S1. Motivation for fabricating freestanding Ag_2Se/CNT films

In the conventional preparation of flexible thermoelectric materials, the thermoelectric material is typically deposited onto polymer substrates such as PI or Nylon. However, this approach has three inherent limitations:

1. **Limitations on thickness and flexibility:** When thermoelectric materials rely on polymer substrates to achieve flexibility, the thickness of the material deposited on a PI film is typically limited to the submicron range to maintain overall flexibility, while the thickness of materials vacuum-filtered onto a nylon substrate is generally less than 5 μm after hot pressing. This results in high internal resistance, which limits power output.

2. **Limitations of power density:** Although the polymer substrates used (~50 μm Nylon or PI) are relatively thin, they are still an order of magnitude thicker than the thermoelectric layer. While the power density of the thermoelectric material layer alone is relatively high, the polymer substrate and thermoelectric material are integrated as a single unit to achieve flexibility, resulting in a lower overall practical power density.

3. **Limitations of functionality:** Thermoelectric materials prepared on polymer substrates often have their performance and functionality constrained by the substrate itself, making it difficult to meet diverse application requirements. In contrast, flexible freestanding films can be encapsulated with various substrates, allowing flexible selection for specific application scenarios and significantly broadening their applicability. For example, poly(*α*-lipoic acid) (PLA) flexible substrates can meet the recyclability requirements of wearable devices; polyimide (PI) flexible substrates satisfy the bendability and thermal stability demands of wearable devices; polydimethylsiloxane (PDMS) flexible substrates are suitable for skin-conformal self-powered sensing patches; and medical-grade polyurethane (PU) or polycaprolactone (PCL) biocompatible substrates are suitable for implantable sensors, meeting the requirements for long-term safety and tissue compatibility.

Note S2. The formula used to calculate the work function.

$$\Phi = h\nu - (E_{cutoff} - E_F)$$

where Φ is the work function, $h\nu$ is the incident photon energy (21.22 eV for He I), E_{cutoff} is the secondary electron cutoff energy, and E_F is the Fermi level.

Note S3. Calculation of Orientation Factors.

The preferred orientation factor F is determined using the following equation:

$$F = (P\text{-}P_0)/(1\text{-}P_0)$$

$$P = \sum I_{(00l)}/\sum I_{(hkl)}$$

$$P_0 = \sum I_{0(00l)}/\sum I_{0(hkl)}$$

where $I_{(00l)}$ represents the sum of the diffraction intensity of (00l) planes, $\sum I_{(hkl)}$ denotes the total intensity of all (hkl) diffraction peaks and P is the ratio of the (00l) plane intensity in the measured data. The $\sum I_{0(00l)}$, $\sum I_{0(hkl)}$, and P_0 correspond to the respective values from the standard pattern.

Note S4. Heat-balance discussion for sap flow monitoring.

1. Experimental control of boundary conditions:

The entire simulated stem segment housing the sensor was encapsulated by a foam insulation layer and an outermost aluminum foil reflective shield.

2. Heat-balance equation and order-of-magnitude estimation:

Based on the control volume of the heated simulated stem segment, the general steady-state heat balance equation is:

$$q_{heater} = q_{advection} + q_{axial} + q_{radial\text{-}loss}$$

where $q_{advection}$ represents the convective heat carried away by the sap flow; q_{axial} represents the net axial heat conduction along the stem, which depends on the stem's thermal resistance and the temperature gradient; $q_{radial\text{-}loss}$ represents the radial heat loss from the stem surface to the environment, including convection and radiation through the encapsulation layers.

Because the thermocouples are symmetrically placed relative to the heating point, and the stem segment is homogeneous with symmetric boundary conditions, the axial temperature distribution is symmetric under no-flow conditions, resulting in negligible net axial conduction. When sap flow is present, the symmetry is broken; however, under steady flow conditions, q_{axial} remains constant and is of a smaller magnitude compared to the advection-induced temperature difference. Therefore, in the subsequent calibration, the influence of q_{axial} is implicitly absorbed into the empirical constants and does not compromise the monotonic relationship between ΔT and flow rate.

Radial heat loss $q_{radial\text{-}loss}$ is the primary pathway for environmental disturbances. In our experiment, this term was significantly reduced through physical encapsulation

Foam layer (thickness d ≈ 1 cm, thermal conductivity k ≈ 0.03 W/(m·K)) provides the dominant thermal resistance. The equivalent heat transfer coefficient is U ≈ k/d ≈ 3 W/(m^2·K). Compared to a bare stem exposed to natural convection (typical h ≈ 10 - 50 W/(m^2·K)), the driving coefficient for radial heat loss is suppressed by at least one order of magnitude.

Aluminum foil reflective shield (reflectivity > 0.9) blocks incoming short-wave solar radiation and ambient long-wave radiation, rendering the radiative heat exchange negligible.

Sealing of the encapsulation also prevents moisture exchange between the measurement section and the atmosphere, thereby eliminating evaporative latent heat loss from the stem surface.

Under these conditions, even when ambient wind speed, humidity, or light intensity vary, the residual fluctuation in $q_{radial\text{-}loss}$ is substantially smaller than $q_{advection}$ and can be treated as a

quasi-constant background term.

3. Simplification of the thermal physics:

With constant heating power, suppressed radial heat loss, and a stable axial conduction term, the heat-balance equation simplifies to:

$$q_{\text{heater}} - q_{\text{axial}} - q_{\text{radial-loss}} \approx q_{\text{advection}}$$

The left-hand side can be regarded as a quasi-constant “effective heating power.” For sap flow, $q_{\text{advection}} = \dot{m} c_p \Delta T$, where $\dot{m}$ is the mass flow rate, c_p is the specific heat capacity of the fluid, and ΔT is the temperature difference measured by the upstream and downstream thermocouples.

Thus, under constant heating and stable background heat losses, ΔT exhibits a well-defined monotonic relationship with $\dot{m}$ (approximately linear at low flow rates). By using a peristaltic pump to impose precise flow rates and recording the corresponding ΔT, we established the sensor’s calibration curve. This calibration inherently incorporates the combined effects of the stem’s intrinsic thermal resistance, residual radial heat loss, and axial conduction, making it valid for similar stem materials under identical encapsulation conditions.

Supplemental Tables

Table S1. |S|, *PF*, *σ* of flexible freestanding TE materials via solution processing at ~300 K.

Material	$\|S\|$ ($\mu V\ K^{-1}$)	σ ($S\ cm^{-1}$)	*PF* ($\mu W\ cm^{-1}\ K^{-2}$)	Ref.
MoS_2/CNT	68	235	1.1	1
Ag_2Se/nylon	135	38	0.7	2
PVDF/Ag_2Se	96	206	1.9	3
PEDOT: PSS/$Bi_{0.5}Sb_{1.5}Te_3$	44	774	1.5	4
PEDOT-Tos/Te/SWCNT	48	432	1.3	5
$Bi_{0.5}Sb_{1.5}Te_3$/PVDF	274	17	1.3	6
Bi_2Te_3/SWCNT	100	520	5.2	7
Cu-BST/PEDOT: PSS	37	2264	3.1	8
Ag_2Se	127	341	5.5	9
Ag_2Se-NW-film	128	757	12.4	9
Ta_4SiTe_4/PVDF	247	94	5.8	10
$Ag_{1.8}Se$/CNT	143	869	17.8	**This work**

Table S2. Radius, and σ/σ_0 of flexible freestanding TE materials via solution processing after bending cycles at ~300 K.

Material	Radius (mm)	Bending cycles	σ/σ_0	Ref.
MoS_2/CNT	1	200	0.92	1
Ag_2Se/nylon	4	2000	0.915	2
PVDF/Ag_2Se	8	1000	0.842	3
PEDOT: PSS/$Bi_{0.5}Sb_{1.5}Te_3$	16.5	1200	0.98	4
PEDOT-Tos/Te/SWCNT	1.5	100	0.99	5
$Bi_{0.5}Sb_{1.5}Te_3$/PVDF	8	1000	0.8	6
Bi_2Te_3/SWCNT	2.5	200	0.99	7
Cu-BST/PEDOT: PSS	2	-	-	8
Ag_2Se	4	1000	0.96	9
Ag_2Se-NW-film	4	500	0.90	9
Ta_4SiTe_4/PVDF	4.5	5000	0.99	10
$Ag_{1.8}Se$/CNT	2	20000	0.95	**This work**
$Ag_{1.8}Se$/CNT	1	1000	0.97	**This work**

Table S3. Comparison of the *PF* of representative TE materials and the *P* of their corresponding devices.

Material	Substrate	*PF* ($\mu W\ cm^{-1}\ K^{-2}$)	*P* (μW)	N	Size (mm)	R (Ω)	ΔT (K)	Ref.
$Ag_2Se_{1-\delta}$/Ag	PI	24.0	0.58	9	18*10*0.0008	352	20	11
$Ag_{1.8}Se$	PI	17.0	0.07	4	20*5*0.0005	415	20	12
Ag_2Se (Te)	PI	21.0	0.07	2	20*4*0.00024	140	20	13
$Ag_{2.19}Se$	PI	23.3	0.11	7	20*2.5*0.0008	603	20	14
Ag_2Se (Cu)	PI	20.8	0.2	6	20*5*0.0005	667	20	15
Ag_2Se	PI	25.9	0.24	4	16*5*0.001	120	20	16
$Ag_{2.02}Se$	PI	19.5	0.17	8	46*2.5*0.00045	2628	20	17
Ag_2Se/Ag/CuAgSe	Nylon	22.3	0.12	6	20*5*0.0003	69.7	18	18
PC/Ag2Se/CuAgSe	Nylon	16.0	1.16	11	25*5*0.007	140	21	19
Ag_2Se/Se/PPy	Nylon	22.4	0.79	6	20*5*0.0036	78	21.7	20
PEI/Ag_2Se	Nylon	22.4	0.35	6	30*4*0.0015	280	20	21
Ag_2Se	Freestanding	5.5	0.38	5	20*3*0.01	253	20	9
$Ag_{1.8}Se$/CNT	Freestanding	17.8	2.33	5	18*4*0.01	22	20	**This work**

Table S4. Source data for the multi-dimensional performance comparison of this work with representative TE materials and devices.

Material	Methods* (Score#)	$P_d^{max}L/(\Delta T)^2$ ($\mu W\ cm^{-1}\ K^{-2}$)	Electricity (kWh)	r (mm)	Temperature (K)	Ref.
Ag_2Se -foil	HR (4)	3.52	~600	3	1323	22
Bi_2Te_3 (Te 7.5%)	SP+ Ann (1)	1.8	~41	5	723	23
$Bi_{0.4}Sb_{1.6}Te_3$	VTE + Ann (3)	1.50	~16	5	673	24
$Ag_{1.8}Se$/CNT	VF+HP (5)	4.63	~7.6	1	413	**This work**

*HR: hot-rolling; SP: screen-printed; Ann: annealing; VTE: vacuum thermal evaporation; VF: vacuum filtration; HP: hot pressing.

#**Qualitative scores of Methods**

The score in the brackets (from 1 to 5) reflects the accessibility of the equipment required for each preparation method, considering primarily cost and availability, with higher scores indicating lower cost and greater commonality. The key equipment for the preparation of Ag_2Se foil includes tube furnaces and hot rolling mills, both of which are common in laboratories. The total cost is approximately $14,000, which is moderately priced. The main equipment for the preparation of Bi_2Te_3 (7.5%) is the spark plasma sintering system, which is relatively rare in laboratories and costs approximately $140,000, making it quite expensive. The core equipment

for the preparation of $Bi_{0.4}Sb_{1.6}Te_3$ is the vacuum evaporation coating system, which is a commonly used instrument in laboratories. It costs about $25,000 and is relatively expensive. The main equipment used in this study is a small benchtop hot press, which is widely applied in laboratories and has a cost of approximately $1,400, making it relatively inexpensive.

Table S5. Feed and actual element ratios of Ag_xSe/CNT samples.

Sample	Ag (%)	Se (%)	Ag:Se
$Ag_{1.0}Se$	48.230	51.770	0.932
$Ag_{1.2}Se$	53.726	46.274	1.161
$Ag_{1.4}Se$	56.327	43.673	1.290
$Ag_{1.6}Se$	62.050	37.950	1.635
$Ag_{1.8}Se$	66.608	33.392	1.995

Table S6. Comparison of the normalized power density at maximum output power of this work with some representative F-TEGs.

Material	P_d (W m^{-2})	L* (cm)	ΔT (K)	$P_d^{max}L/(\Delta T)^2$ (μW cm^{-1} K^{-2})	Ref.
Ag_2Se	5.4	1.6	30	0.96	9
Ag_2Se-foil	167	1.0	68.9	3.52	22
Ag_2Se/Nylon	0.47	2.6	40.6	0.074	2
PVDF/Ag_2Se	0.01	1.2	30	0.0013	3
PEDOT:PSS/$Bi_{0.5}Sb_{1.5}Te_3$	0.45	1.7	50	0.03	4
$Ag_2S_{0.5}Se_{0.5}$	0.08	1.1	20	0.022	25
PEDOT-Tos/Te/SWCNT	2.62	1.3	60	0.095	5
Ag_2Se/Carbon	22.9	1.6	31.4	3.72	26
$Ag_2Se_{1-\delta}$/Ag	8.07	1.5	20	3.03	11
$Ag_{1.8}Se$	46.8	1.4	50	2.62	12
Ag_2(S, Se)-Ag_2Se	26.5	1.7	50	1.8	27
Ag_2Se/Ag/CuAgSe	5.42	2.0	45	0.54	18
Bi_2Te_3 (Te)	12.0	0.6	20	1.8	24
$Bi_{0.4}Sb_{1.6}Te_3$	69.0	0.7	56.8	1.50	25
Ag_2Se/PI	11.3	0.6	40	0.42	28
Ag_2Se	2.3	1.5	30	0.38	29
Ag_2Se	3.2	0.4	40	0.80	30
PVP@Ag_2Se/MC	22.1	1.7	36.1	2.88	31
$Ag_{2.3}Se$	5.8	1.0	25	0.93	32
Ag_2Se/PVP	31.2	1.6	38.7	3.33	33
$Ag_{1.98}S_{1/3}Se_{1/3}Te_{1/3}$	14.3	1.5	30	2.38	34
Ag/Ag_2Se	13.5	1.4	29.6	2.16	35
Ag_2Se/rGO	67.0	0.45	26	4.46	36
$Ag_{1.8}Se$/CNT	77.1	1.5	50	4.63	**This work**

Supplementary Figures

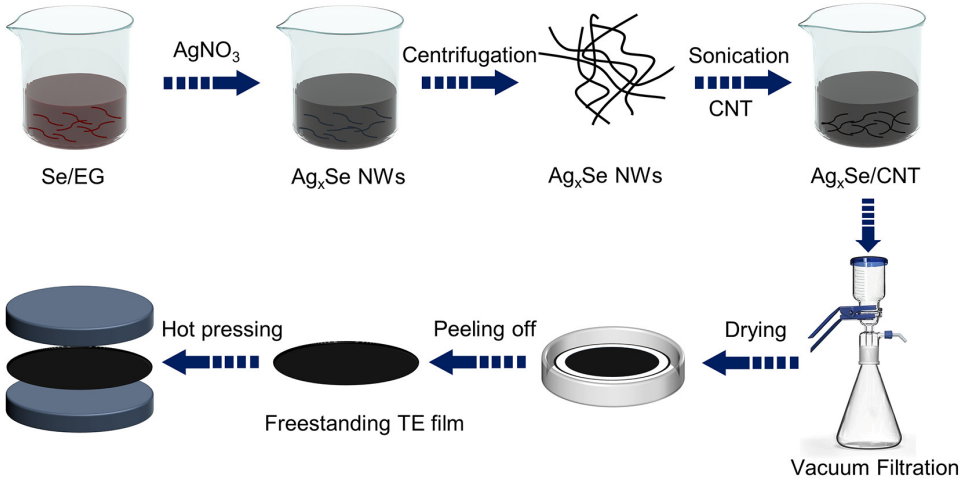

Figure S1. Schematic illustration of the synthesis process of Ag_xSe/CNT composite films.

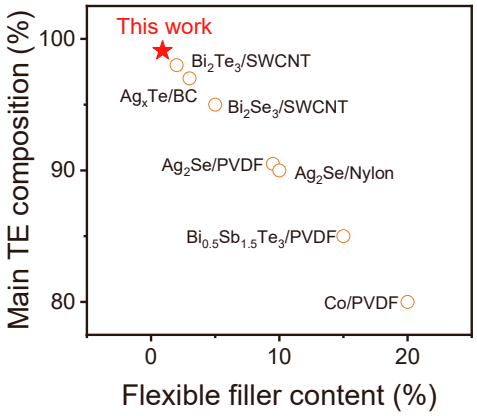

Figure S2. Comparison of the maximum load-bearing capabilities of our freestanding $Ag_{1.8}Se$/CNT composite films with other reported freestanding thermoelectric (TE) materials.[3, 6, 7, 37-40]

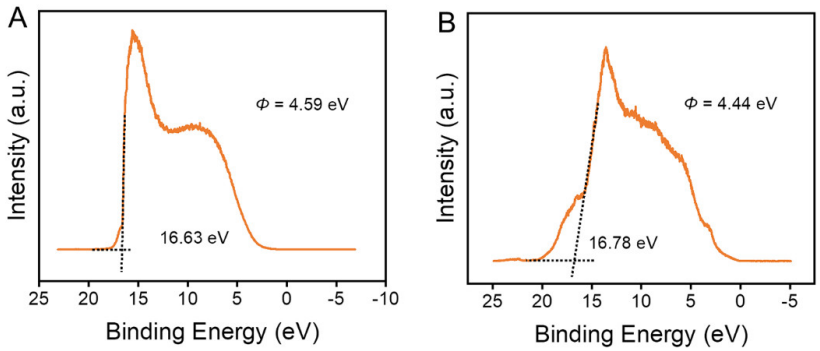

Figure S3. Work function measurements based on UPS analysis. (**A**) $Ag_{1.8}Se$ film, (**B**) CNT film.

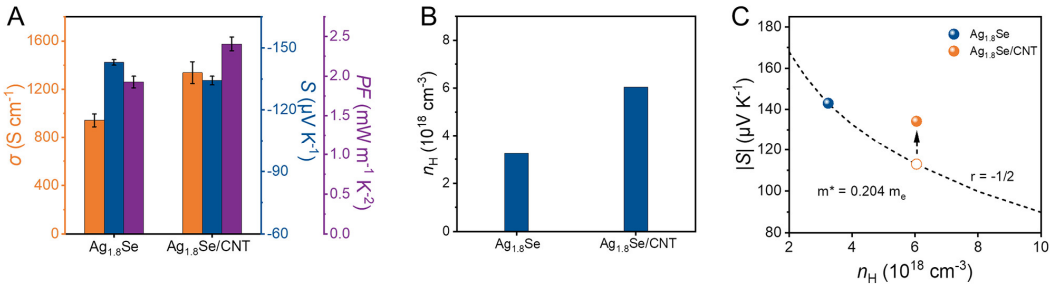

Figure S4. Electrical transport properties of $Ag_{1.8}Se$ and $Ag_{1.8}Se$/CNT (CNT: 0.9 wt%) films prepared on nylon substrates. (**A**) Thermoelectric properties. (**B**) Carrier concentration (n_H). (**C**) Seebeck coefficient ($|S|$) as a function of carrier concentration. The deviation of $|S|$ for the $Ag_{1.8}Se$/CNT composite from the theoretical curve serves as direct evidence for the interfacial energy filtering effect. The potential barriers formed at the numerous $Ag_{1.8}Se$/CNT interfaces effectively scatter or block low-energy carriers while allowing high-energy carriers to pass through. This process increases the average energy of the participating charge carriers, thereby compensating for the expected drop in $|S|$ caused by the increased n_H.

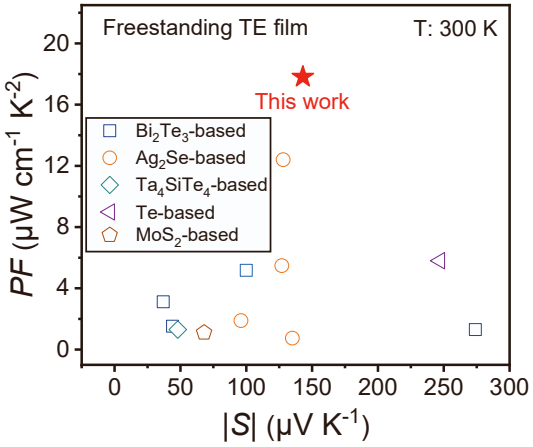

Figure S5. Room temperature *PF* as a function of absolute Seebeck coefficient $|S|$ for freestanding TE films via solution processing.[1-10]

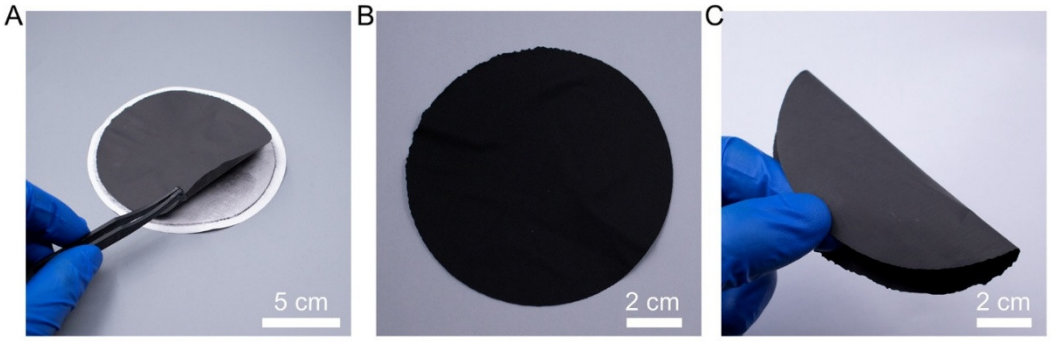

Figure S6. Large-area, flexible, freestanding $Ag_{1.8}Se$/CNT composite film: (**A**) being lifted from a nylon substrate, (**B**) a freestanding flat film, (**C**) a freestanding film bent to demonstrate flexibility.

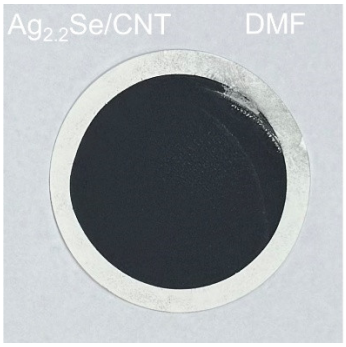

Figure S7. Photograph of an $Ag_{2.2}Se$/CNT film prepared with 0.9 wt.% CNT using DMF as the dispersant, showing difficulty in peeling from a nylon substrate.

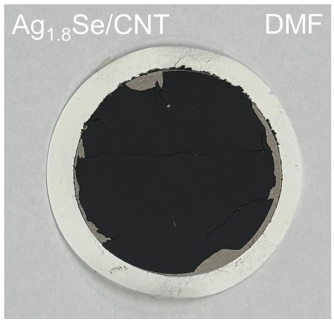

Figure S8. Photograph of an $Ag_{1.8}Se$/CNT film prepared with 0.8 wt.% CNT using DMF as the dispersant, showing difficulty in peeling from a nylon substrate.

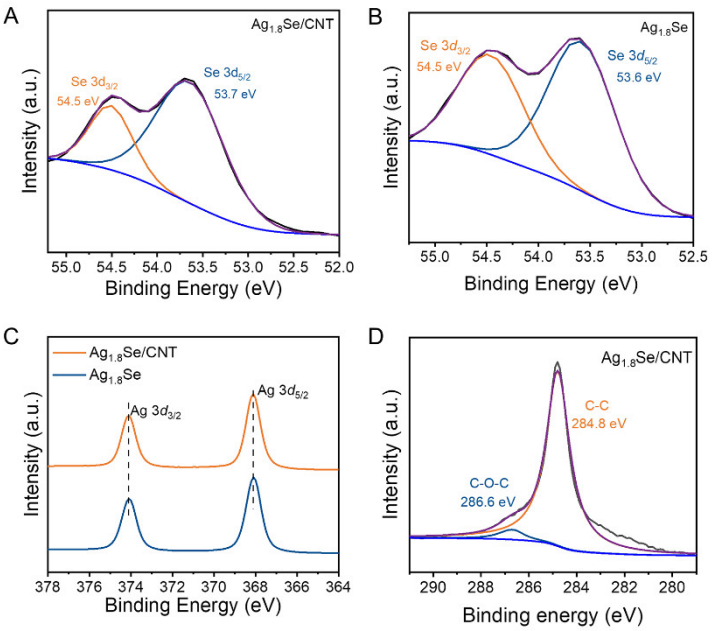

Figure S9. XPS spectra of $Ag_{1.8}Se$/CNT and $Ag_{1.8}Se$ films. (**A**) Se 3*d* core-level spectra for the $Ag_{1.8}Se$/CNT film, (**B**) Se 3*d* core-level spectra for the $Ag_{1.8}Se$ film, (**C**) Ag 3*d* core-level spectra for the $Ag_{1.8}Se$ and $Ag_{1.8}Se$/CNT film, (**D**) C 1*s* core-level spectra for the $Ag_{1.8}Se$/CNT film.

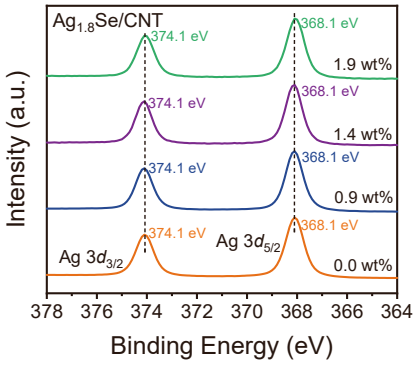

Figure S10. XPS comparison of $Ag_{1.8}Se$/CNT samples with varying CNT contents.

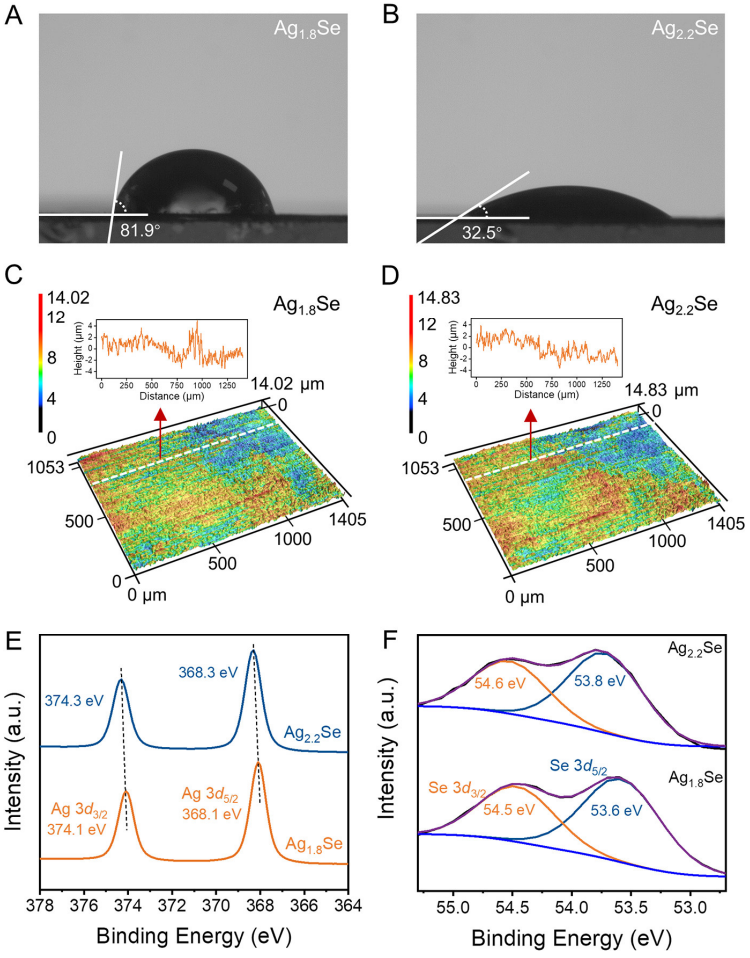

Figure S11. Surface characteristics and chemical states of the $Ag_{1.8}Se$ and $Ag_{2.2}Se$. (**A** and **B**) Water contact angles of $Ag_{1.8}Se$ (**A**) and $Ag_{2.2}Se$ (**B**) films. the contact angle decreases from 81.9° to 32.5°, indicating a substantial increase in surface energy and hydrophilicity. (**C** and **D**) 3D laser-scanning confocal microscopy images of the surface morphology of $Ag_{1.8}Se$ (**C**) and $Ag_{2.2}Se$ (**D**) films. Insets: Cross-section profiles along the lines. These results confirm that both samples exhibit nearly identical surface roughness; therefore, the influence of geometric roughness on the contact angle can be excluded. (**E** and **F**) High-resolution Se 3*d* (**E**) and Ag 3*d* (**F**) core-level spectra of the $Ag_{1.8}Se$ and $Ag_{2.2}Se$ powders. The Ag XPS peak exhibits a 0.2 eV positive shift, suggesting a modified surface chemical environment.

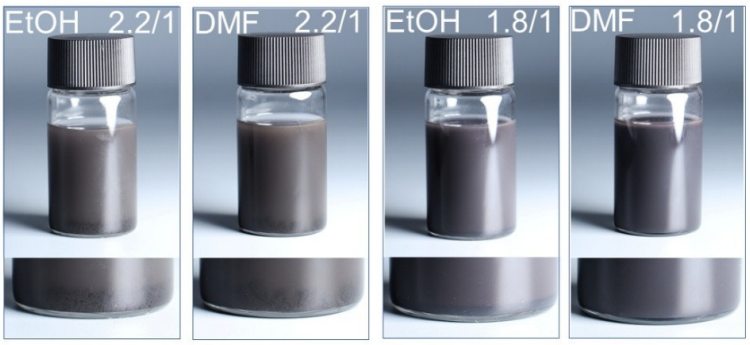

Figure S12. Dispersion behavior of Ag_xSe nanowires with various Ag/Se molar ratios following sonication (1 h) in EtOH and DMF. $Ag_{2.2}Se$ exhibits pronounced agglomeration after ultrasonication in both EtOH and DMF, whereas $Ag_{1.8}Se$ shows partial agglomeration in EtOH but remains stably dispersed in DMF following ultrasonication.

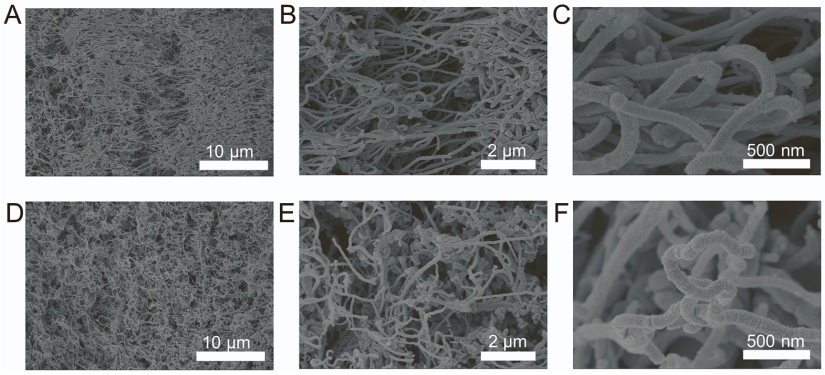

Figure S13. Low-magnification to high-magnification cross-sectional SEM images of $Ag_{1.8}Se$/CNT composite films prepared using different dispersion solvents before hot pressing. (**A-C**) EtOH. (**D-F**) DMF.

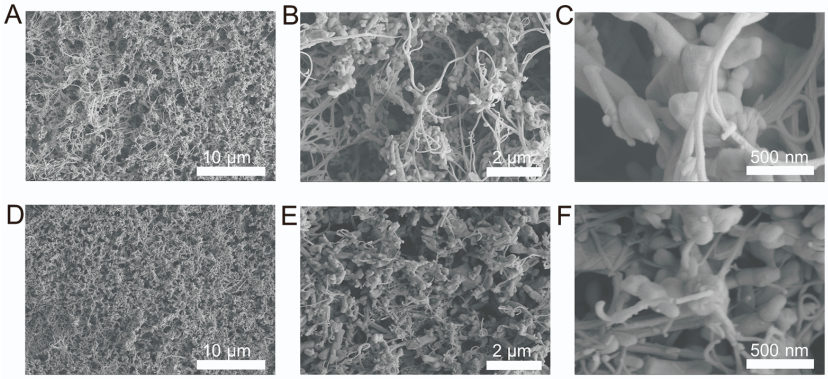

Figure S14. Low-magnification to high-magnification surface SEM images of $Ag_{1.8}Se$/CNT composite films prepared using different dispersion solvents before hot pressing. (**A-C**) EtOH. (**D-F**) DMF.

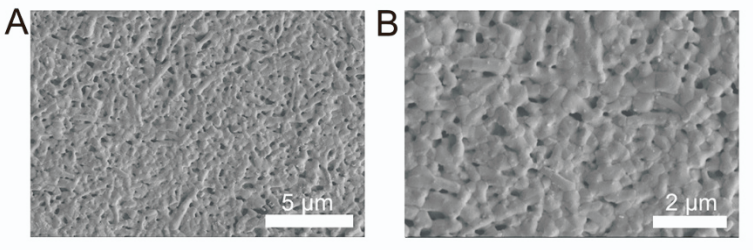

Figure S15. (**A** and **B**) Surface SEM images of $Ag_{1.8}Se$ films after hot pressing at different magnifications.

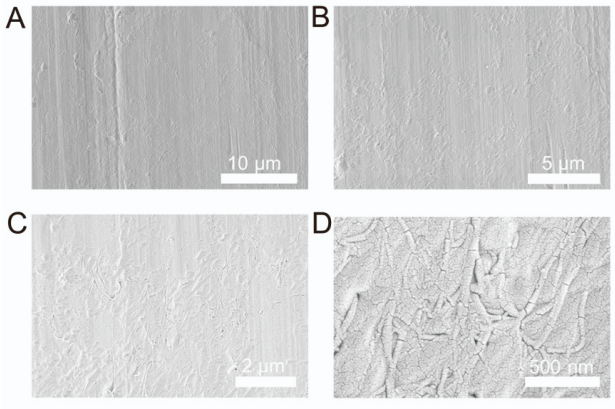

Figure S16. (**A-D**) Surface SEM images of $Ag_{1.8}Se$/CNT films after hot pressing at different magnifications.

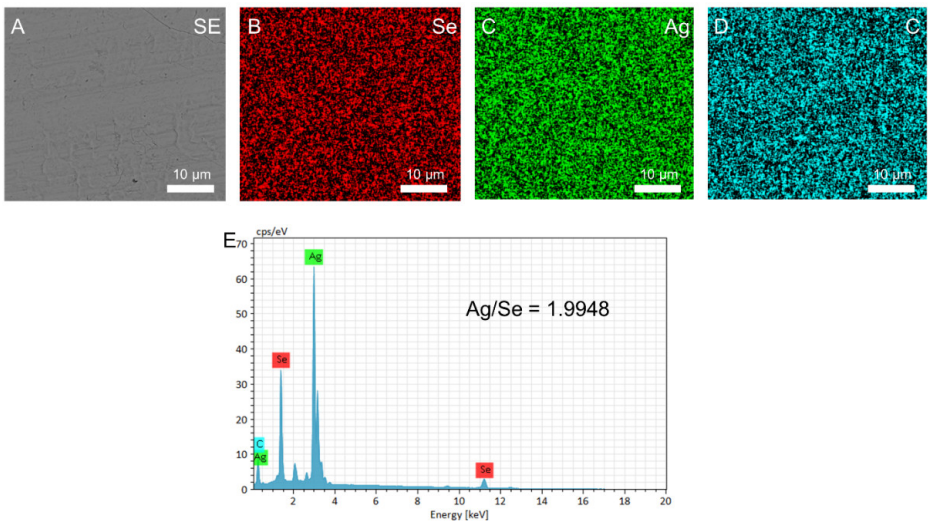

Figure S17. Characterizations of compositions of $Ag_{1.8}Se$/CNT composite films. (**A-D**) SE surface SEM image of $Ag_{1.8}Se$/CNT film and the corresponding EDS maps of (**B**) Se, (**C**) Ag, and (**D**) C. (**E**) Measured atomic ratio of Ag/Se in the $Ag_{1.8}Se$/CNT composite film.

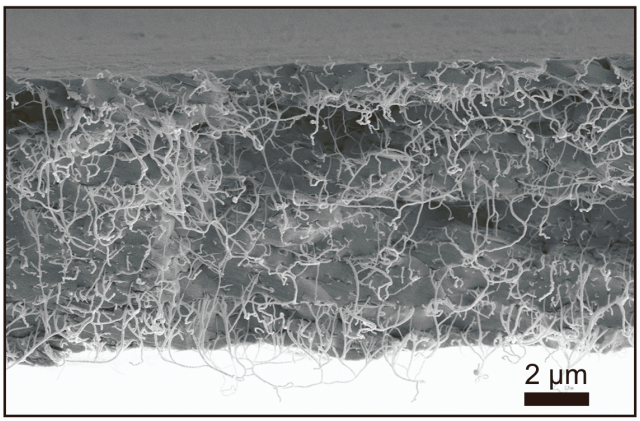

Figure S18. Cross-sectional SEM image of $Ag_{1.8}Se$/CNT composite film after hot pressing. To better display the structural details of the CNTs, the cross-section was prepared by direct snapping at room temperature, rather than by liquid nitrogen–assisted brittle fracture.

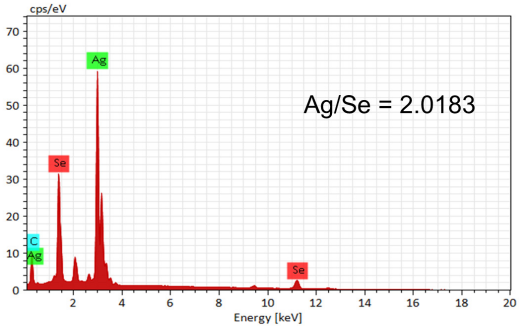

Figure S19. Measured atomic ratio of Ag/Se in the $Ag_{1.8}Se$/CNT composite film obtained from cross-sectional EDS mapping.

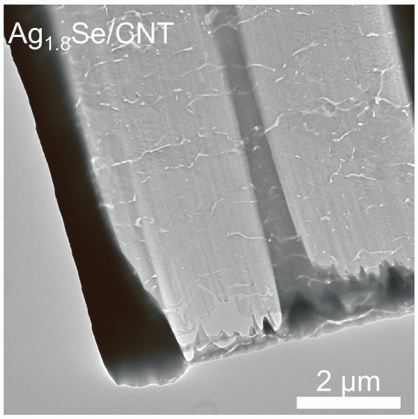

Figure S20. Overview TEM image of the $Ag_{1.8}Se$/CNT composite.

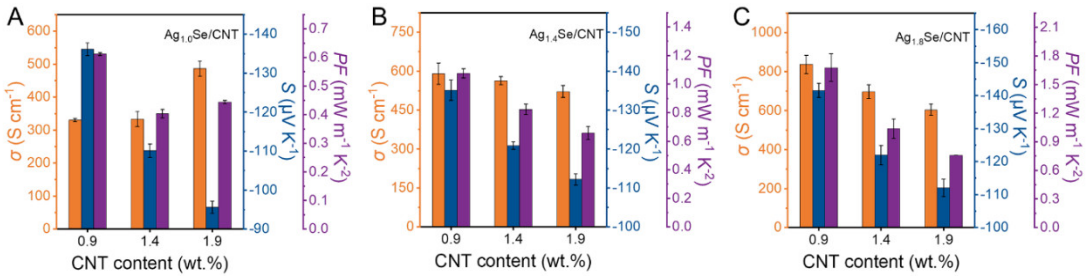

Figure S21. Thermoelectric properties of Ag_xSe/CNT composite films at different CNT contents. (**A**) x = 1.0. (**B**) x = 1.4. (**C**) x = 1.8.

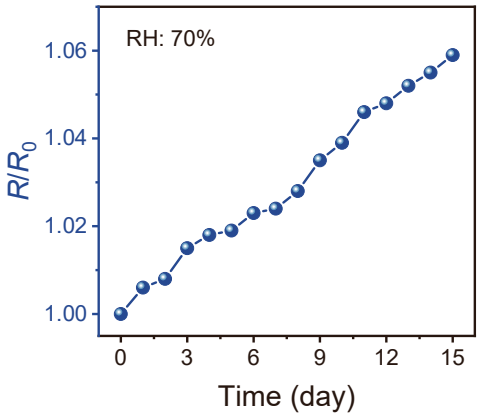

Figure S22. Resistance change of $Ag_{1.8}Se$/CNT film over 15 consecutive days at 70% humidity.

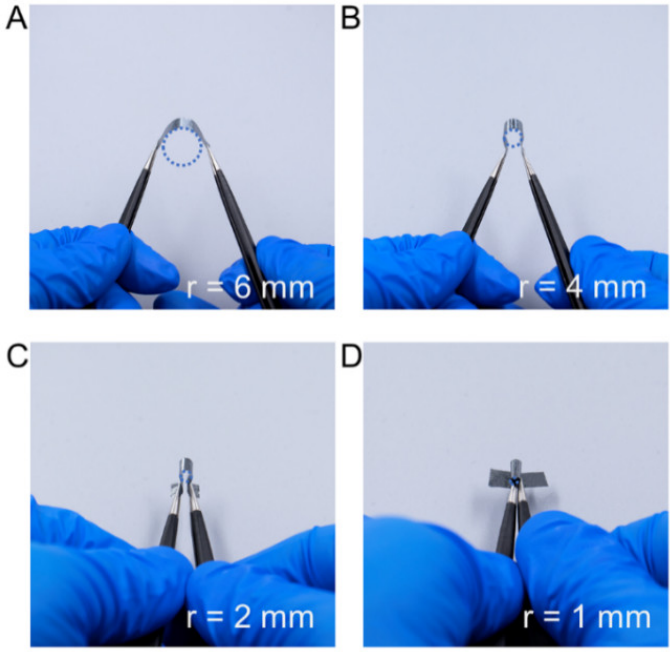

Figure S23. Photographs of $Ag_{1.8}Se$/CNT composite films under different bending radii. (**A**) 6 mm. (**B**) 4 mm. (**C**) 2mm. **(D)** 1mm.

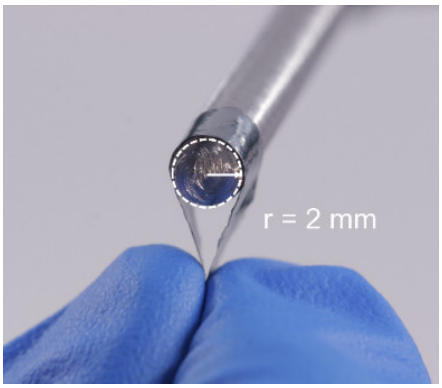

Figure S24. Setup of the 2 mm bending test for $Ag_{1.8}Se$/CNT composite films.

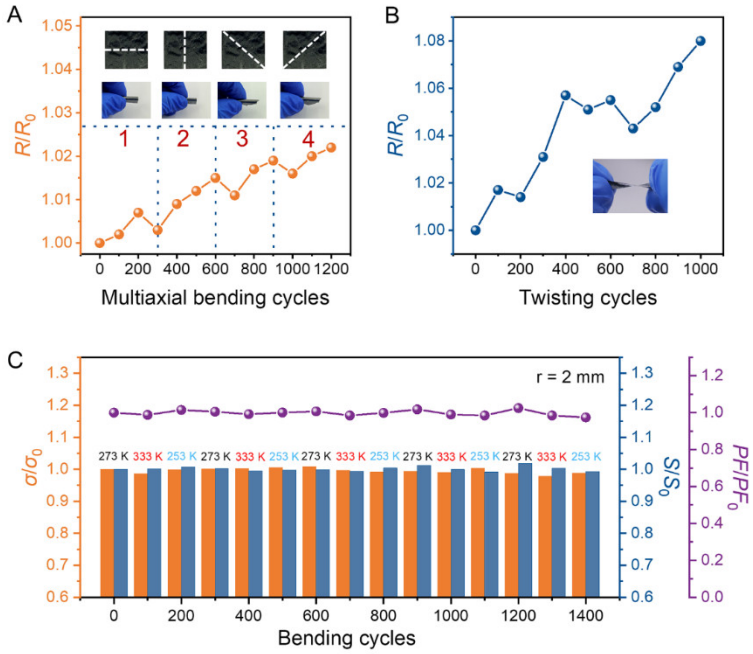

Figure S25. Performance stability of $Ag_{1.8}Se$/CNT composite films under different deformation modes. (**A**) multi-axis bending, (**B**) twisting, and (**C**) coupled thermal-mechanical loading.

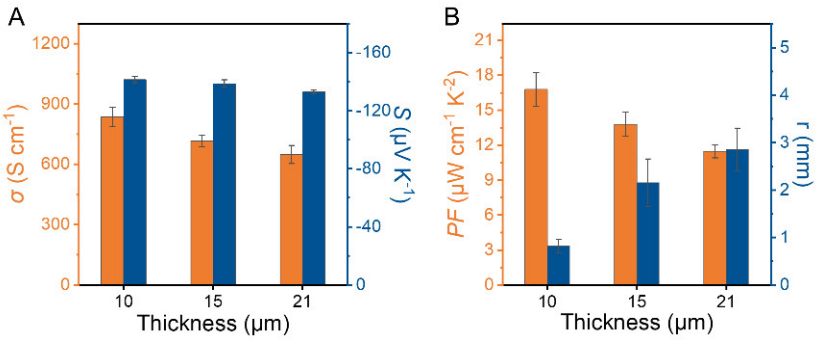

Figure S26. Thermoelectric properties and flexibility of $Ag_{1.8}Se$/CNT composite films with varying thicknesses. (**A**) σ and S at different thicknesses, (**B**) PF and bending radius (r) at different thicknesses.

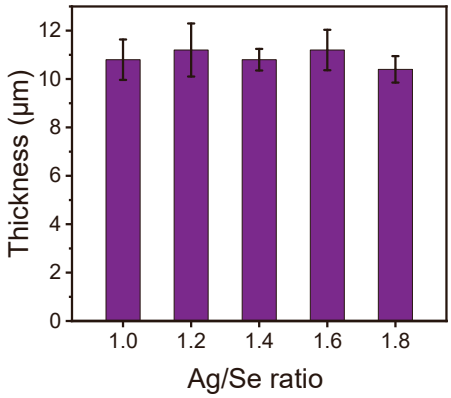

Figure S27. Thickness of Ag_xSe/CNT composite films with different Ag/Se ratios.

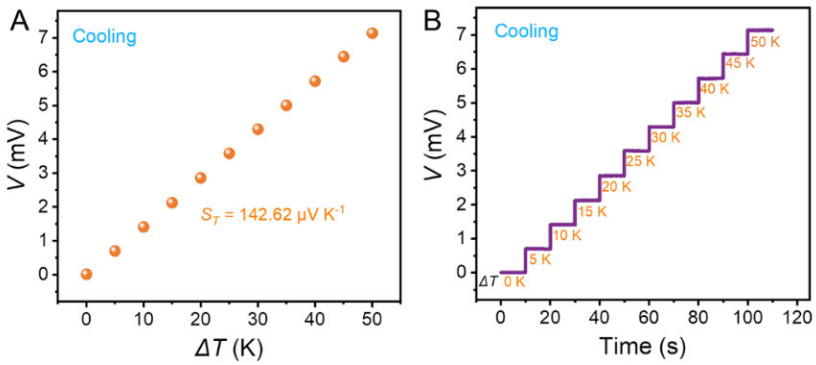

Figure S28. Variation of the *V* of a single $Ag_{1.8}Se$/CNT thermoelectric leg during the cooling process. (**A**) Output *V* at different *ΔT*. (**B**) Stable and continuous *V* output as a function of time.

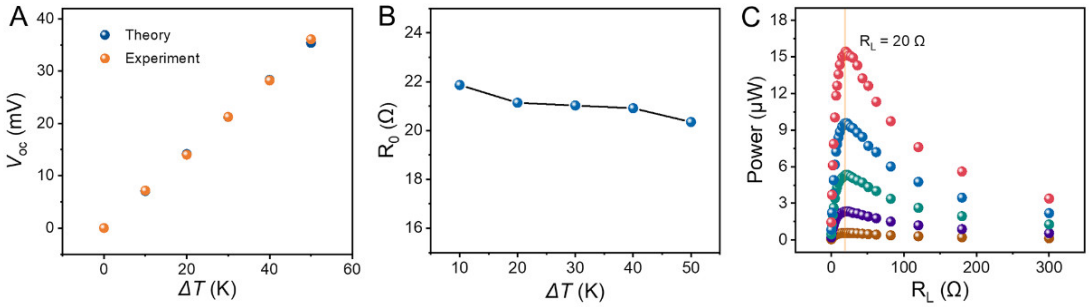

Figure S29. Performance of the F-TEG composed of five series-connected $Ag_{1.8}Se$/CNT legs under varying *ΔT* and load resistance (R_L). (**A**) Calculated and tested V_{oc} of the device at different *ΔT*. $V_{Theory} = NS\Delta T$, where *N* is the number of thermoelectric legs. (**B**) Internal resistance (R_0) of the device as a function of *ΔT*. (**C**) *P* at different external R_L.

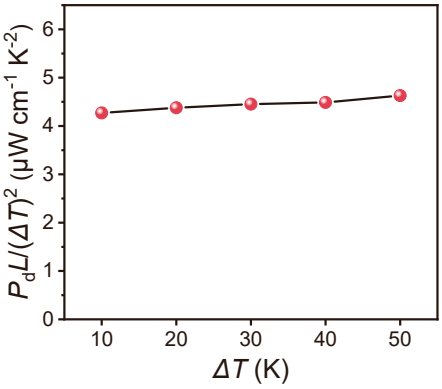

Figure S30. Normalized power density of the F-TEG at different ΔT.

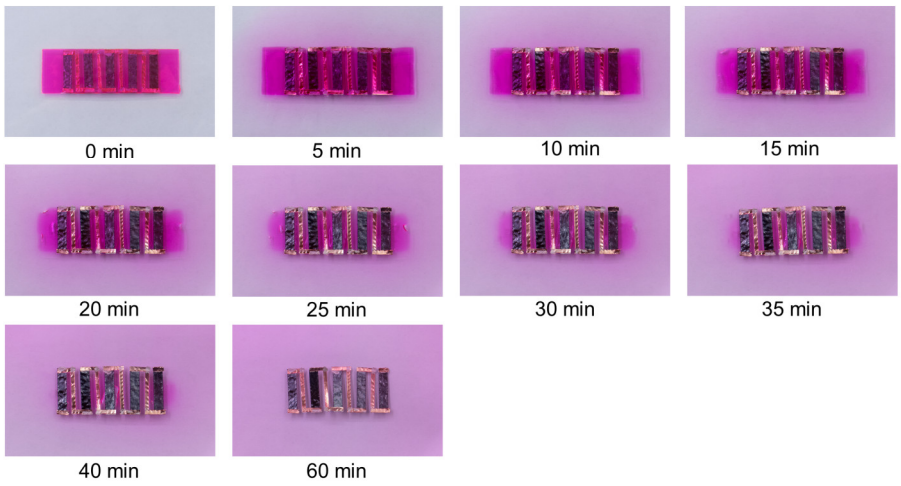

Figure S31. Photographs showing the dissolution of poly(α-lipoic acid) (PLA) in water during the recycling of the F-TEG. The PLA film was prepared using the solution casting method. Specifically, 2 g of (alpha-)lipoic acid and 0.8 g of Tris(hydroxymethyl)aminomethane were dissolved in 20 mL of ultrapure water and stirred at 65 °C for 5 minutes. The resulting solution was poured into a mold, and the PLA film was formed after slow water evaporation at room temperature.

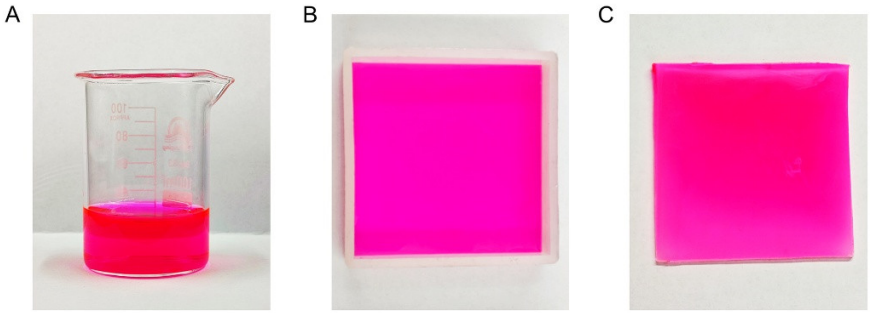

Figure S32. Photographs of the PLA recycling process. (**A**) Collected PLA aqueous solution. (**B**) PLA solution cast into a mould for drying. (**C**) Recycled PLA film.

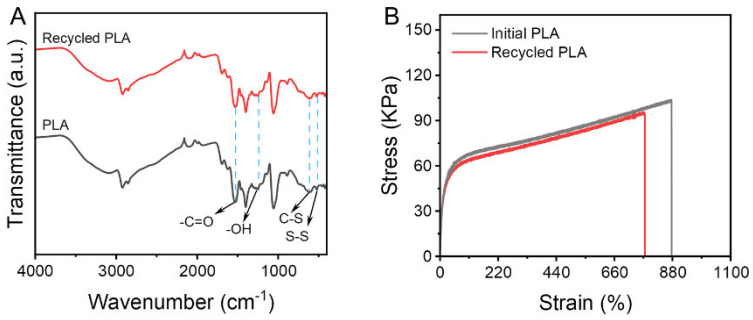

Figure S33. Stability evaluation of the PLA film during recycling. (**A**) Fourier transform infrared (FTIR) spectra of the PLA films before and after recycling. (**B**) stress-strain curves of the PLA films before and after recycling. FTIR spectra and stress-strain curves of PLA films before and after recycling show no significant changes.

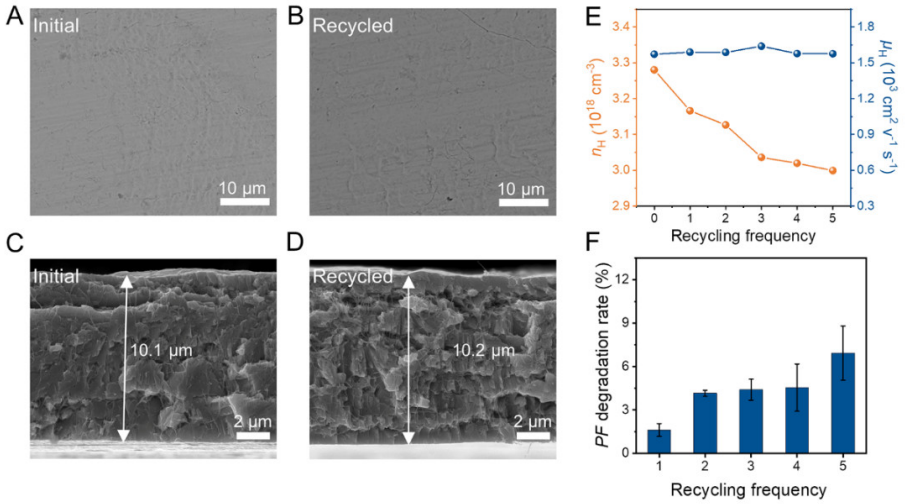

Figure S34. Microstructural and electrical stability of the material after five recycling cycles. (**A**, **B**) Surface SEM images of the initial material (**A**) and after (**B**) 5 recycling cycles. (**C**, **D**) Cross-sectional SEM images before (**C**) and after (**D**) 5 recycling cycles. (**E**) Evolution of carrier concentration and carrier mobility during the recycling process. (**F**) Calculated performance degradation rate after 5 recycling cycles.

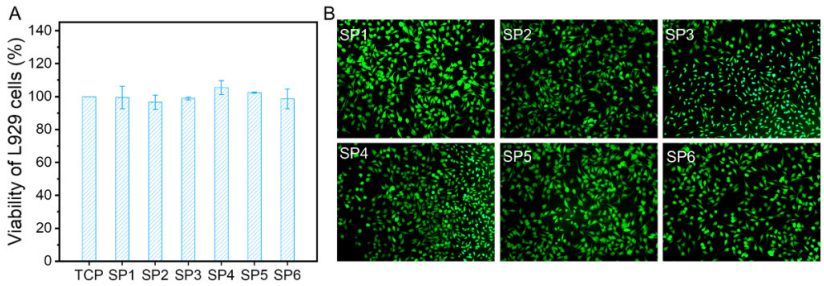

Figure S35. Biocompatibility of $Ag_{1.8}Se$/CNT Composite Film. (**A**) The Viability of L929 cells cultured for 1 day in the extract solution of the $Ag_{1.8}Se$/CNT composite film. (**B**) Live/dead staining of L929 cells cultured for 24 hours in the extract solution of the $Ag_{1.8}Se$/CNT composite film.

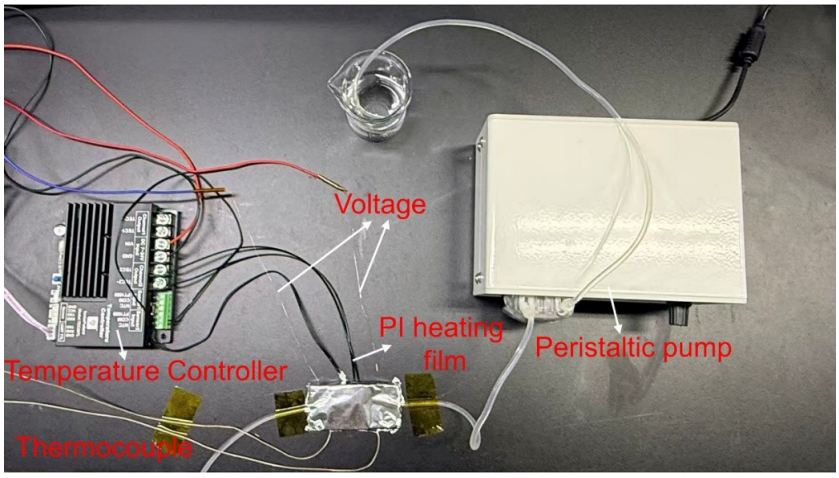

Figure S36. Photograph of the custom experimental apparatus for simulated sap flow monitoring.

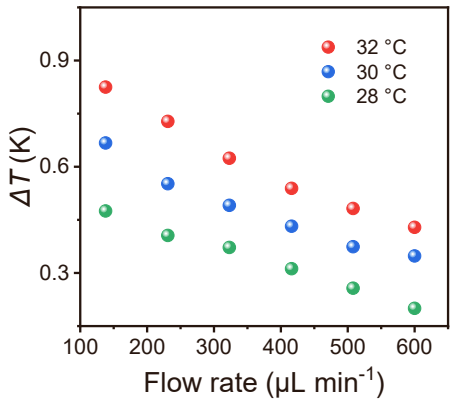

Figure S37. Plot of ΔT versus sap flow at different heating temperatures. The ΔT increases as the sap flow rate decreases and rises with increasing heating temperature.

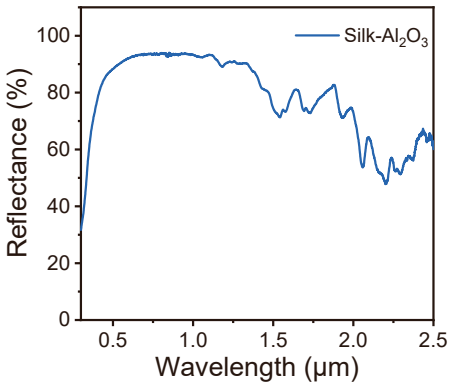

Figure S38. Reflectivity spectrum of Al_2O_3-doped silk fabric in the 0.3-2.5 μm wavelength range. The high reflectivity of the fabric across the full solar spectrum (0.3-2.5 μm), combined with the intrinsic high emissivity of silk in the wavelength range of 8-13 μm, enables excellent radiative cooling performance.

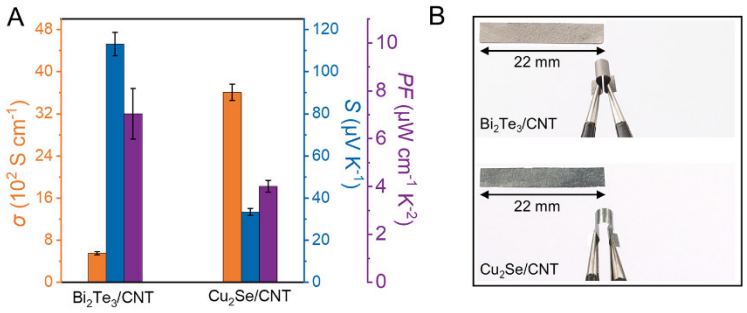

Figure S39. Thermoelectric properties and flexibility of Bi_2Te_3/CNT and Cu_2Se/CNT composite films. (**A**) *σ*, *S*, and *PF* of Bi_2Te_3/CNT and Cu_2Se/CNT composite films. (**B**) Photographs of bent Bi_2Te_3/CNT and Cu_2Se/CNT composite films with a radius less than 2 mm.

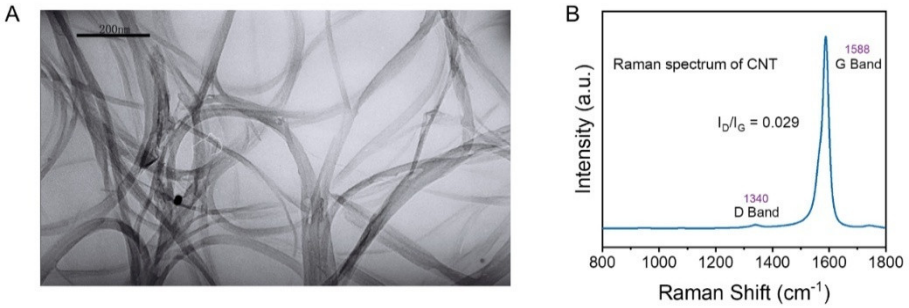

Figure S40. Structural characterization of CNTs. (**A**)TEM image, and (**B**) Raman spectrum of CNT. The CNTs we employ are a commercial product with diameters ranging from 1-2 nm, lengths between 5-30 μm, and are single-walled. Raman spectrum indicates an I_D/I_G ratio of 0.029, demonstrating a high graphitization degree and low defect levels.

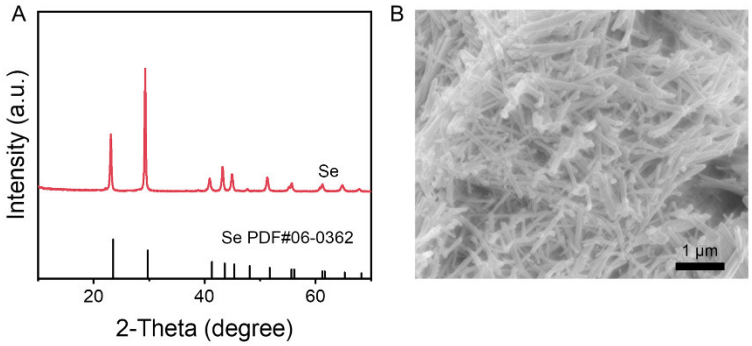

Figure S41. Phase, structure of nanowires. (**A**) XRD patterns of Se nanowires. (**B**) SEM of Se nanowires.

Supplemental References

[S1]. Li, J., Shi, Q., Rohr, J., Wu, H., Wu, B., Guo, Y., Zhang, Q., Hou, C., Li, Y., and Wang, H. (2020). Flexible 3D porous MoS_2/CNTs architectures with ZT of 0.17 at room temperature for wearable thermoelectric applications. Adv. Funct. Mater. *30*, 2002508. https://doi.org/10.1002/adfm.202002508.

[S2]. Li, J., Liu, Y., Wang, Z., Chen, L., and Cai, K. (2023). Ultra-flexible self-supporting Ag_2Se/nylon composite films for wearable thermoelectric devices. Compos. Part B Eng. *265*, 110946. https://doi.org/10.1016/j.compositesb.2023.110946.

[S3]. Zhou, H., Zhang, Z., Sun, C., Deng, H., and Fu, Q. (2020). Biomimetic approach to facilitate the high filler content in free-standing and flexible thermoelectric polymer composite films based on PVDF and Ag_2Se nanowires. ACS Appl. Mater. Interfaces *12*, 51506–51516. https://doi.org/10.1021/acsami.0c15414.

[S4]. Sun, L., Ao, D., Hwang, J., Liu, Q., Cao, E., and Sun, B. (2024). Realizing high thermoelectric performance flexible free-standing PEDOT:PSS/$Bi_{0.5}Sb_{1.5}Te_3$ composite films for power generation. Rare Met. *43*, 5985–5993. https://doi.org/10.1007/s12598-024-02860-0.

[S5]. Liang, L., Wang, M., Wang, X., Peng, P., Liu, Z., Chen, G., and Sun, G. (2022). Initiating a Stretchable, Compressible, and Wearable Thermoelectric Generator by a Spiral Architecture with Ternary Nanocomposites for Efficient Heat Harvesting. Adv. Funct. Mater. *32*, 2111435. https://doi.org/10.1002/adfm.202111435.

[S6]. Na, Y., Kim, S., Mallem, S.P.R., Yi, S., Kim, K.T., and Park, K.-I. (2022). Energy harvesting from human body heat using highly flexible thermoelectric generator based on Bi_2Te_3 particles and polymer composite. J. Alloy. Compd. *924*, 166575. https://doi.org/10.1016/j.jallcom.2022.166575.

[S7]. Chen, Z., Lv, H., Zhang, Q., Wang, H., and Chen, G. (2022). Construction of a cement-rebar nanoarchitecture for a solution-processed and flexible film of a Bi_2Te_3/CNT hybrid toward low thermal conductivity and high thermoelectric performance. Carbon Energy *4*, 115–128. https://doi.org/10.1002/cey2.161.

[S8]. Wang, Y., Hong, M., Liu, W., Shi, X., Xu, S., Sun, Q., Gao, H., Lu, S., Zou, J., and Chen, Z. (2020). $Bi_{0.5}Sb_{1.5}Te_3$/PEDOT: PSS-based flexible thermoelectric film and device. Chem. Eng. J. *397*, 125360. https://doi.org/10.1016/j.cej.2020.125360.

[S9]. Wang, H., Lin, X., Han, G., Zhang, B., Chen, Y., Zhang, L., Lu, X., Wang, G., and Zhou, X. (2025). Flexible porous Ag_2Se films: From freestanding inorganic films to inorganic-network/organic-skeleton thermoelectric generators. Adv. Funct. Mater. *35*. 2413605. https://doi.org/10.1002/adfm.202413605.

[S10]. Xu, Q., Qu, S., Ming, C., Qiu, P., Yao, Q., Zhu, C., Wei, T., He, J., Shi, X., and Chen, L. (2020). Conformal organic-inorganic semiconductor composites for flexible thermoelectrics. Energy Environ. Sci. *13*, 511–518. https://doi. org/10.1039/c9ee03776d.

[S11]. Cao, T., Shi, X., Hu, B., Yang, Q., Lyu, W., Sun, S., Yin, L., Liu, Q., Chen, W., Wang, X., et al. (2025). Advancing Ag_2Se thin-film thermoelectrics via selenization-driven anisotropy control. Nat. Commun. *16*, 1555. https://doi.org/10.1038/s41467-025-56671-7.

[S12]. Hou, S., Liu, Y., Yin, L., Chen, C., Wu, Z., Wang, J., Luo, Y., Xue, W., Liu, X., Zhang, Q., and Cao, F. (2021). High performance wearable thermoelectric generators using Ag_2Se

films with large carrier mobility. Nano Energy *87*, 106223. https://doi.org/10.1016/j.nanoen.2021.106223.

[S13]. Yang, D., Shi, X., Li, M., Nisar, M., Mansoor, A., Chen, S., Chen, Y., Li, F., Ma, H., Liang, G., et al. (2024). Flexible power generators by Ag_2Se thin films with record-high thermoelectric performance. Nat. Commun. *15*, 923. https://doi.org/10.1038/s41467-024-45092-7.

[S14]. Chen, Y., Shi, X., Zhang, J., Nisar, M., Zha, Z., Zhong, Z., Li, F., Liang, G., Luo, J., Li, M., et al. (2024). Deviceization of high-performance and flexible Ag_2Se films for electronic skin and servo rotation angle control. Nat. Commun. *15*, 8356. 10.1038/s41467-024-52680-0.

[S15]. Hou, S., Liu, Y., Luo, Y., Wang, X., Yin, L., Sun, X., Wu, Z., Wang, J., Li, M., Chen, Z., et al. (2022). High-performance, thin-film thermoelectric generator with self-healing ability for body-heat harvesting. Cell Rep. Phys. Sci. *3*, 101146. https://doi.org/10.1016/j.xcrp.2022.101146.

[S16]. Lei, Y., Qi, R., Chen, M., Chen, H., Xing, C., Sui, F., Gu, L., He, W., Zhang, Y., Baba, T., et al. (2022). Microstructurally tailored thin β-Ag_2Se films toward commercial flexible thermoelectrics. Adv. Mater. *34*, 2104786. https://doi.org/10.1002/adma.202104786.

[S17]. Zheng, Z., Li, Y., Niu, J., Wei, M., Zhang, D., Zhong, Y., Nisar, M., Abbas, A., Chen, S., Li, F., et al. (2022). Significantly (00l)-textured Ag_2Se thin films with excellent thermoelectric performance for flexible power applications. J. Mater. Chem. A *10*, 21603–21610. https://doi.org/10.1039/d2ta06356e.

[S18]. Lu, Y., Qiu, Y., Cai, K., Ding, Y., Wang, M., Jiang, C., Yao, Q., Huang, C., Chen, L., and He, J. (2020). Ultrahigh power factor and flexible silver selenide-based composite film for thermoelectric devices. Energy Environ. Sci. *13*, 1287–1288. https://doi.org/10.1039/d0ee90012e.

[S19]. Lu, Y., Qiu, Y., Cai, K., Li, X., Gao, M., Jiang, C., and He, J. (2020). Ultrahigh performance PEDOT/Ag_2Se/CuAgSe composite film for wearable thermoelectric power generators. Mater. Today Phys. *14*, 100223. https://doi.org/10.1016/j.mtphys.2020.100223.

[S20]. Li, Y., Lou, Q., Yang, J., Cai, K., Liu, Y., Lu, Y., Qiu, Y., Lu, Y., Wang, Z., Wu, M., et al. (2022). Exceptionally high power factor Ag_2Se/Se/polypyrrole composite films for flexible thermoelectric generators. Adv. Funct. Mater. *32*, 2106902. https://doi.org/10.1002/adfm.202106902.

[S21]. Hu, Q., Liu, W., Zhang, L., Gao, H., Wang, D., Wu, T., Shi, X., Li, M., Liu, Q., Yang, Y., and Chen, Z. (2024). Carrier separation boosts thermoelectric performance of flexible n-type Ag_2Se-based films. Adv. Energy Mater. *14*. 2401890. https://doi.org/10.1002/aenm.202401890.

[S22]. Ding, W., Shen, X., Jin, M., Hu, Y., Chen, Z., Meng, E., Luo, J., Li, W., and Pei, Y. (2024). Robust bendable thermoelectric generators enabled by elasticity strengthening. Nat. Commun. *15*, 9767. https://doi.org/10.1038/s41467-024-54084-6.

[S23]. Chen, W., Shi, X., Li, M., Liu, T., Mao, Y., Liu, Q., Dargusch, M., Zou, J., Lu, G., and Chen, Z. (2024). Nanobinders advance screen-printed flexible thermoelectrics. Science *386*, 1265–1271. https://doi.org/10.1126/science.ads5868.

[S24]. Mao, D., Zhou, Y., Yu, Y., Wang, Y., Han, M., Meng, Q., Lu, Y., Feng, J., Kong, M., Yang, H., et al. (2024). Scalable and sustainable manufacturing of twin boundary-enhanced flexible $Bi_{0.4}Sb_{1.6}Te_3$ films with high thermoelectric performance. Joule *8*. 3313-3323. https://doi.org/10.1016/j.joule.2024.08.009.

[S25]. Liang, J., Wang, T., Qiu, P., Yang, S., Ming, C., Chen, H., Song, Q., Zhao, K., Wei, T., Ren, D., et al. (2019). Flexible thermoelectrics: From silver chalcogenides to full-inorganic devices. Energy Environ. Sci. *12*, 2983–2990. https://doi.org/10.1039/c9ee01777a.

[S26]. Zhang, M., Li, J., Liu, Y., Liu, Y., Huang, C., Liu, R., Wei, P., Zhao, W., Xie, W., Weidenkaff, A., and Cai, K. (2025). Screen printing high-performance free-standing Ag_2Se/carbon composite film for flexible thermoelectric converters. Nano Energy *138*, 110836. https://doi.org/10.1016/j.nanoen.2025.110836.

[S27]. Wu, H., Shi, X., Li, M., Gao, H., Liu, W., Zhu, M., Yin, L., Wang, D., Duan, J., Chen, Z., and Liu, Q. (2025). Sandwich engineering advances ductile thermoelectrics. Adv. Mater. *37*. 2503020. https://doi.org/10.1002/adma.202503020.

[S28]. Kumar, S., Battabyal, M., Sethupathi, K., and Satapathy, D. (2024). High-performance printed Ag_2Se/PI flexible thermoelectric film for powering wearable electronics. Appl. Mater. Interfaces *16*, 40848–40857. https://doi.org/10.1021/acsami.4c05537.

[S29]. Ding, Y., Qiu, Y., Cai, K., Yao, Q., Chen, S., Chen, L., and He, J. (2019). High performance n-type Ag_2Se film on nylon membrane for flexible thermoelectric power generator. Nat. Commun. *10*, 841. https://doi.org/10.1038/s41467-019-08835-5.

[S30]. Liu, Y., Zhang, Q., Huang, A., Zhang, K., Wan, S., Chen, H., Fu, Y., Zuo, W., Wang, Y., Cao, X., et al. (2024). Fully inkjet-printed Ag_2Se flexible thermoelectric devices for sustainable power generation. Nat. Commun. *15*, 2141. https://doi.org/10.1038/s41467-024-46183-1.

[S31]. Qin, J., Du, Y., Meng, Q., Chen, S., Hong, M., and Ke, Q. (2025). Versatile polymer-coated Ag_2Se thermoelectric materials and devices for multi-scenario applications developed by direct-ink printing. Nat. Commun. *16*, 8497. https://doi.org/10.1038/s41467-025-63390-6.

[S32]. Gao, J., Miao, L., Lai, H., Zhu, S., Peng, Y., Wang, X., Koumoto, K., and Cai, H. (2020). Thermoelectric flexible silver selenide films: Compositional and length optimization. Iscience *23*, 100753. https://doi.org/10.1016/j.isci.2019.100753.

[S33]. Lu, Y., Han, X., Wei, P., Liu, Y., Wang, Z., Zuo, X., Zhao, W., and Cai, K. (2024). Nanoengineering approach toward ultrahigh power factor Ag_2Se/polyvinylpyrrolidone composite film for flexible thermoelectric generator. Chem. Eng. J. *485*, 149793. https://doi.org/10.1016/j.cej.2024.149793.

[S34]. Chen, H., Shao, C., Huang, S., Gao, Z., Huang, H., Pan, Z., Zhao, K., Qiu, P., Wei, T., and Shi, X. (2024). High-entropy cubic pseudo-ternary Ag_2(S, Se, Te) materials with excellent ductility and thermoelectric performance. Adv. Energy Mater. *14*. 2303473. https://doi.org/10.1002/aenm.202303473.

[S35]. Li, X., Lu, Y., Cai, K., Gao, M., Li, Y., Wang, Z., Wu, M., Wei, P., Zhao, W., Du, Y., and Shen, S. (2022). Exceptional power factor of flexible Ag/Ag_2Se thermoelectric composite films. Chem. Eng. J. *434*, 134739. https://doi.org/10.1016/j.cej.2022.134739.

[S36]. Zhang, L., Shi, X., Shang, H., Gu, H., Chen, W., Li, M., Huang, D., Dong, H., Wang, X., Ding, F., and Chen, Z. (2025). High-performance Ag_2Se-based thermoelectrics for wearable electronics. Nat. Commun. *16*, 5002. https://doi.org/10.1038/s41467-025-60284-5.

[S37]. Yang, Z., Jin, X., Wang, W., Huang, C., Lei, Y., and Wang, Y. (2022). Ag_2Se/nylon self-supporting composite films for wearable photo-thermoelectric generators with high output characteristics. J. Mater. Chem. A *10*, 21080–21092. https://doi.org/10.1039/d2ta06064g.

[S38]. Chen, Y., He, M., Tang, J., Bazan, G., and Liang, Z. (2018). Flexible thermoelectric generators with ultrahigh output power enabled by magnetic field-aligned metallic nanowires. Adv. Electron. Mater. *4*, 1800200. https://doi.org/10.1002/aelm.201800200.

[S39]. Zhang, L., Shang, H., Huang, D., Xie, B., Zou, Q., Gao, Z., Xue, J., Gu, H., and Ding, F. (2022). N-type flexible Bi_2Se_3 nanosheets/SWCNTs composite films with improved thermoelectric performance for low-grade waste-heat harvesting. Nano Energy *104*, 107907. https://doi.org/10.1016/j.nanoen.2022.107907.

[S40]. Yu, P., Feng, L., Tang, W., Liu, C., Lan, J., Lin, Y., and Yang, X. (2023). Robust, flexible thermoelectric film for energy harvesting by a simple and eco-friendly method. ACS Appl. Mater. Interfaces *15*, 13144–13154. https://doi.org/10.1021/acsami.3c00118.